A nonparametric Bayesian analysis of independent and identically distributed observations of covariate-driven Poisson processes

Patric Dolmeta[*]
ESOMAS Department, University of Turin
and
Matteo Giordano
ESOMAS Department, University of Turin

Abstract

An important task in the statistical analysis of inhomogeneous point processes is to investigate the influence of covariates on the point-generating mechanism. In this article, we consider the nonparametric Bayesian approach, assuming that n independent and identically distributed realizations of the point pattern and the covariate random field are available. We employ hierarchical prior distributions based on multi-bandwidth Gaussian processes, and prove that the resulting posterior distributions concentrate around the ground truth at optimal rate as $n \to \infty$, achieving automatic adaptation to the possibly anisotropic smoothness. Posterior inference is concretely implemented via a Metropolis-within-Gibbs Markov chain Monte Carlo algorithm that incorporates an ad-hoc sampling scheme to handle the functional component of the proposed nonparametric Bayesian model. Our theoretical results are supported by extensive numerical simulation studies. Further, we present an application to the analysis of a Canadian wildfire dataset.

Keywords. Anisotropic function; Cox process; Inhomogeneous Poisson process; Metropolis within Gibbs; Multi-bandwidth Gaussian process; Posterior contraction rate

Contents

[*] M.G. has been partially supported by MUR, PRIN project 2022CLTYP4. The authors gratefully acknowledge the support from the "de Castro" Statistics Initiative.

1 Introduction

Inhomogeneous point processes are primary mathematical models to describe the distribution of events that take place randomly over space and time. In many applications, the occurrence of the events is determined, or heavily influenced, by covariates. It is then of interest to investigate the relationship between the points and the covariates. This can be mathematically formalized as an intensity estimation problem in the following way: Let N be a point process over some Euclidean domain $\mathcal{W}$, and for any $A \subseteq \mathcal{W}$, denote by $N(A)$ the number of events within A. The (first-order) intensity function of N is a map $\lambda : \mathcal{W} \to [0, \infty)$ with the property that $\mathrm{E}[N(A)] = \int_A \lambda(x)dx$, and N is said to be inhomogeneous if λ is non-constant. Additionally, let $Z = \{Z(x),\ x \in \mathcal{W}\}$ be a multivariate field, with values in some subset $\mathcal{Z} \subseteq \mathbb{R}^d$, $d \in \mathbb{N}$, representing the measurements of the covariates at each location in the domain. The connection between

N and Z is then customarily modeled by assuming that the intensity be driven by the covariates, namely that

$$\lambda(x) = \rho(Z(x)), \qquad x \in \mathcal{W}, \tag{1}$$

for some unknown function $\rho : \mathcal{Z} \to [0, \infty)$. Note that this formulation allows for 'purely spatial' effects by listing the 'coordinates' of x within the covariates $Z(x)$. The goal is to estimate ρ from observations of N and Z. Such covariate-based intensity estimation problems arise in a variety of scientific fields, including environmental statistics (e.g. Borrajo et al. (2020)), geology (e.g. Baddeley et al. (2012)) and ecology (e.g. Guan (2008)), to mention a few. See Section 4 for an application to the task of predicting the location of wildfires via meteorological covariates.

When the covariates are (all or partly) random, the resulting point process is termed 'doubly stochastic'. In particular, we will focus on the case where the overarching point-generating mechanism is of Poisson type, whereby N defines a Cox process, Cox (1955). In this framework, covariate-based intensity estimation has been widely studied under parametric models for the function ρ in (1), both in the frequentist (e.g. Brillinger (1978), Diggle (1990), Waagepetersen (2007)) and Bayesian literature (e.g. Rue et al. (2009), Yue & Loh (2011), Illian et al. (2012)). Further see the monograph Diggle (2014), where many more references can be found. For instance, the celebrated log-Gaussian Cox model, Møller et al. (1998), postulates that Z be a multivariate Gaussian process, and that $\lambda(x) = e^{\beta^T Z(x)}$ for some vector $\beta \in \mathbb{R}^d$.

In contrast, the nonparametric literature on the subject is considerably less developed. The first frequentist investigation in this context was by Guan (2008), who constructed covariate-based kernel-type procedures. They derived asymptotic point-wise consistency results under the assumption that Z is a stationary and ergodic random field, in an 'increasing domain' asymptotic regime in which the volume of the observation window $\mathcal{W}$ diverges and a single realization of N and Z over $\mathcal{W}$ is observed. Similar estimators were later defined by Baddeley et al. (2012) and by Borrajo et al. (2020), and were studied under related sampling schemes.

Nonparametric Bayesian methods for intensity estimation have so far been almost exclusively confined to non-covariate-driven point processes. Seminal methodological advances were provided by, among the others, Lo (1982), Kuo & Ghosh (1997), DiMatteo et al. (2001), Kottas & Sansó (2007), Adams et al. (2009), covering a variety of prior distributions, ranging from gamma processes-based ones, to beta process, kernel mixture, spline and Gaussian process priors, respectively. Building on the landmark developments in the theory of Bayesian nonparametrics from the early 2000s, Ghosal et al. (2000), several articles have investigated the asymptotic convergence properties of nonparametric Bayesian procedures in models without covariates. Belitser et al. (2015) developed the Hellinger testing approach for independent and identically distributed (i.i.d.) observations of an inhomogeneous Poisson process over a fixed domain, and employed it to derive minimax optimal posterior contraction rates towards Hölder-smooth intensities for spline priors with uniform coefficients. These results were extended to Gaussian process priors by Kirichenko & van Zanten (2015) under similar i.i.d. sampling schemes; see also Gugushvili & Spreij (2013). Procedures with piecewise-constant priors were investigated by Gugushvili et al. (2018). Lastly, Donnet et al. (2017) obtained optimal performance guarantees for general Aalen point processes under various types of smoothness and shape constraints.

To our knowledge, the only existing study of covariate-based nonparametric Bayesian intensity estimation is in the recent article by Giordano et al. (2025), who derived optimal global and local rates for several classes of prior distributions, in an increasing domain asymptotic regime similar to the aforementioned one considered by Guan (2008).

See also the related contribution by Dolmeta & Giordano (2025). While large observation windows are common in spatial statistics, many natural applications with point processes are confined to fixed domains, and rather entail the availability of multiple observations of the event pattern and the covariates, each carrying individual information that needs to be effectively combined in order to achieve consistent estimates. See Section 4 for a concrete example with yearly data. For this important scenario, the results and proof techniques of Giordano et al. (2025), based on concentration inequalities for stationary and ergodic spatial random fields, do not apply, raising the question as to whether nonparametric Bayesian procedures can perform well also in i.i.d. sampling schemes for covariate-driven point processes. In fact, this case appears to be mostly unexplored also in the frequentist literature, which has thus far primarily focused on settings with a single observation of N and Z, cf. Guan (2008), Baddeley et al. (2012), Borrajo et al. (2020), despite interest in the joint analysis of multiple realizations having been raised since at least Diggle et al. (1991). This gap represents the main motivation for our work, where we will provide methodological and theoretical advances for the nonparametric Bayesian approach to the problem.

1.1 Our contributions

In this article, we develop the first nonparametric Bayesian analysis of i.i.d. observations of covariate-driven Poisson processes. Our approach consists in modeling ρ in (1) via a suitable prior distribution and then forming, via Bayes' theorem, the corresponding posterior, which encodes our updated belief about ρ, providing point estimates and uncertainty quantification. See (Ghosal & Van der Vaart 2017, Chapter 1) for an overview on the nonparametric Bayesian paradigm.

For the specification of the prior, we employ 'multi-bandwidth' Gaussian processes, obtained by scaling stationary covariance functions at different levels along distinct directions; see Section 2.1. This construction is popular in machine learning, including e.g. the widely used Automatic Relevance Determination (ARD) kernel, cf. (Rasmussen & Williams 2005, Chapter 5.1), offering desirable modeling flexibility for 'anisotropic' functions whose variations in response to changes in different inputs may occur at distinct characteristic length-scales, or according to diverse smoothness levels; see Section 1.2 for precise definitions. Multi-bandwidth Gaussian processes were shown by Bhattacharya et al. (2014), in simpler statistical models, to be able to achieve optimal reconstructions over anisotropic function spaces.

In our main theoretical result, Theorem 2.3, we derive optimal posterior contraction rates towards the (possibly anisotropic) true intensity function generating the data, in the asymptotic regime where the number of observed realizations of N and Z increases. The proofs are based on the Hellinger testing approach for i.i.d. sampling schemes, which we specialize to the case of covariate-driven Poisson processes adapting ideas from Belitser et al. (2015) and Kirichenko & van Zanten (2015), and which we then pursue for the proposed multi-bandwidth Gaussian process methods, over anisotropic function spaces. To achieve automatic adaptation to the smoothness of the intensity, which is typically unknown in practice, we employ a hierarchical procedure where we randomize the various hyper-parameters in the prior. In particular, we assign independent hyperpriors, modeling the length-scales in the covariance kernel of the underlying Gaussian process as i.i.d. stochastic powers of gamma random variables. We note that this differs from the construction of Bhattacharya et al. (2014), which prescribes a-priori correlated length-scales.

A second contribution of this work is the exploration of the implementation aspects of the nonparametric Bayesian approach to covariate-based intensity estimation. In Section 2.4, we devise a Markov chain Monte Carlo (MCMC) algorithm to approximately sample from the posterior distribution. This is of Metropolis-within-Gibbs type, alternating draws from the full conditional distributions of the various parameters. It incorporates recent developments from the literature for dimension-robust sampling in nonparametric Bayesian procedures based on Gaussian priors to handle the functional component of the considered statistical model.

To assess our methods in practice, we conducted extensive numerical simulations, presented in Section 3. The empirical results are in close agreement with the theory, illustrating the ability of the proposed procedure to reconstruct the true intensity function in a variety of experimental setups. Moreover, the obtained performances were found to be competitive against a kernel-based alternative estimator. Lastly, in Section 4, we develop an application to a Canadian wildfire dataset containing yearly recordings of hotspots and meteorological conditions, where we observe that our approach leads to a desirable combination of the information across the observation period, while also managing to capture year-specific trends in the spatial distributions of the wildfires.

The rest of the paper is organized as follows: In Section 2, we describe the statistical problem and our approach in details, present our main theoretical results, and outline the MCMC sampler employed for concrete implementation. The numerical simulations and data analysis are presented in Sections 3 and 4, respectively. Section 5 contains a summary and a discussion of some related open problems. The proofs of all the results are deferred to the Supplementary Materials, where additional simulations and more details on the data analysis can also be found.

1.2 Main notation

For positive integers $m \in \mathbb{N}$, we denote m-dimensional vectors of real numbers by $t = (t_1, \dots, t_m) \in \mathbb{R}^m$, intended as column vectors unless otherwise stated. We write $a \wedge b$ and $a \vee b$ for the minimum and maximum between $a, b \in \mathbb{R}$, respectively. We use the symbols $\lesssim$, $\gtrsim$ and $\simeq$ for one- and two-sided inequalities holding up to universal multiplicative constants, and $\propto$ to denote the proportionality of a function with respect to its arguments.

Given a measure space $(\mathcal{T}, \mathfrak{T}, \tau)$ and any $1 \le p \le \infty$, let $L^p(\mathcal{T}, \tau)$ be the Lebesgue space of real-valued p-integrable functions defined on $\mathcal{T}$, equipped with norm $\|\cdot\|_{L^p(\mathcal{T},\tau)}$. When $\mathcal{T} \subseteq \mathbb{R}^m$ and τ equals the Lebesgue measure dt, write shorthand $L^p(\mathcal{T}, \tau) = L^p(\mathcal{T})$.

For $\mathcal{T} \subseteq \mathbb{R}^m$, denote by $C(\mathcal{T})$ the space of continuous functions defined on $\mathcal{T}$, equipped with the sup-norm. For $q \in (0, \infty)$, write $C^q(\mathcal{T})$ for the usual Hölder space of $\lfloor q \rfloor$-times differentiable functions whose $\lfloor q \rfloor^{\text{th}}$ derivative is $(q - \lfloor q \rfloor)$-Hölder continuous, and let $\|\cdot\|_{C^q(\mathcal{T})}$ be the norm of $C^q(\mathcal{T})$. Next, we define the family of anisotropic Hölder spaces, containing functions whose degree of smoothness may be different along distinct directions, cf. (Barron et al. 1999, Section 4.1.3). For all $t \in \mathcal{T}$ and $k = 1, \dots, m$, let $\mathcal{S}_{t,k} := \{s \in \mathbb{R} : (t_1, \dots, t_{k-1}, s, t_{k+1}, \dots, t_m) \in \mathcal{T}\}$, and for any $f \in C(\mathcal{T})$, construct the univariate functions $f_{t,k} : s \mapsto f(t_1, \dots, t_{k-1}, s, t_{k+1}, \dots, t_m)$ defined on $\mathcal{S}_{t,k}$. For a vector $\alpha = (\alpha_1, \dots, \alpha_m) \in (0, \infty)^m$, let $C^\alpha(\mathcal{T})$ be the subset of all functions such that

$$\max_{k=1,\dots,m} \sup_{t \in \mathcal{T}} \|f_{t,k}\|_{C^{\alpha_k}(\mathcal{S}_{t,k})} < \infty.$$

Note that the above definition recovers the traditional (isotropic) Hölder spaces if $\alpha_k = \alpha_h$ for all $h, k = 1, \dots, m$. When there is no risk of confusion, we at times omit the dependence of the function spaces on the underlying domain, writing for example L^p for $L^p(\mathcal{T})$.

2 Multi-bandwidth Gaussian process methods for covariate-based intensities

On a compact 'observation window' $\mathcal{W} \subset \mathbb{R}^D$, $D \in \mathbb{N}$, consider a d-dimensional 'covariate' random field $Z := \{Z(x),\ x \in \mathcal{W}\}$ with values in some 'covariate space' $\mathcal{Z} \subseteq \mathbb{R}^d$, $d \in \mathbb{N}$, and a stochastic point pattern $N := \{X_1, \dots, X_K\}$ arising, conditionally given Z, as an inhomogeneous Poisson process with first-order intensity $\lambda_\rho(x) := \rho(Z(x))$, $x \in \mathcal{W}$, for some unknown (measurable and bounded) function $\rho : \mathcal{Z} \to [0, \infty)$. In other words, N is a Cox process, Cox (1955), directed by the random measure $\lambda_\rho(x)dx$, and we have

$$K|Z \sim \mathrm{Po}\Big(\int_{\mathcal{W}} \lambda_\rho(x)dx\Big), \qquad X_1, \dots, X_K|Z, K \overset{\text{iid}}{\sim} \frac{\lambda_\rho(x)dx}{\int_{\mathcal{W}} \lambda_\rho(x)dx}.$$

For some $n \in \mathbb{N}$, we assume that we observe n i.i.d. copies of the pair (N, Z), denoted by $D^{(n)} := \{(N^{(i)}, Z^{(i)})\}_{i=1}^n$, where $N^{(i)} := \{X_1^{(i)}, \dots, X_{K^{(i)}}^{(i)}\}$. We then seek to estimate ρ from data $D^{(n)}$. Throughout, we denote by $P_\rho^{(n)}$ the law of $D^{(n)}$, by $E_\rho^{(n)}$ the expectation with respect to it, and write $P_\rho := P_\rho^{(1)}$, $E_\rho := E_\rho^{(1)}$. The law $P_\rho^{(n)}$ is absolutely continuous with respect to the distribution P_1 of the standard Poisson case (where $\rho \equiv 1$), with likelihood

$$L^{(n)}(\rho) = \prod_{i=1}^n p_\rho(N^{(i)}, Z^{(i)}), \qquad p_\rho(N, Z) = e^{\sum_{k=1}^K \log \rho(Z(X_k)) - \int_{\mathcal{W}} (\rho(Z(x)) - 1)dx}, \tag{2}$$

see e.g. (Kutoyants 1998, Theorem 1.3).

Remark 2.1 (Repeated observations of covariates and points)**.** *Throughout, we are interested in the setting where multiple realizations of Z and N are available. For example, this is the case in our data analysis in Section 4, where we have access to yearly observations. Depending on the application, different measurement schemes may be relevant, such as ones where multiple point patterns are driven by shared (possibly deterministic) covariates. In other cases, a single realization of a covariate-driven point process with large intensity may be available, giving rise to a so-called 'in-fill' asymptotics. It is not difficult to show that these settings are statistically equivalent to the increasing domain regime recently studied by Giordano et al. (2025), where optimal posterior contraction rates for various nonparametric Bayesian procedures were obtained. See Guan (2008) for an earlier related reference. Here, we focus on i.i.d. sampling schemes for covariate-driven Poisson processes, whose theoretical analysis requires different tools and techniques.*

2.1 The prior model

We adopt the nonparametric Bayesian approach, modeling ρ with a prior Π based on Gaussian processes. To do so, we maintain the (harmless, cf. Remark 2.2) assumption that the covariate space $\mathcal{Z}$ be bounded and convex and introduce the one-to-one parametrization

$$\rho(z) = \rho^* \sigma(w(z)), \qquad z \in \mathcal{Z}, \tag{3}$$

where $\rho^* > 0$ is an upper bound for the values of the intensity, $w : \mathcal{Z} \to \mathbb{R}$ is some unknown function and $\sigma : \mathbb{R} \to [0, 1]$ is a fixed, smooth and strictly increasing link function. Throughout, we employ the sigmoid link $\sigma(t) = (1 + e^{-t})^{-1},\ t \in \mathbb{R}$.

Under (3), we specify Π by assigning independent priors Π_{ρ^*} and Π_W to ρ^* and w, respectively. Specifically, for some fixed $a_{\rho^*}, b_{\rho^*}, c_{\rho^*} > 0$, we take Π_{ρ^*} to be a $\Gamma(a_{\rho^*}, b_{\rho^*})$ distribution truncated to the interval $[0, c_{\rho^*} + \log n]$. Its probability density function (p.d.f., also denoted by Π_{ρ^*}) equals

$$\Pi_{\rho^*}(r) = \frac{b_{\rho^*}^{a_{\rho^*}}}{\gamma(a_{\rho^*}, b_{\rho^*}c_{\rho^*} + b_{\rho^*}\log n)} r^{a_{\rho^*}-1} e^{-b_{\rho^*}r}, \qquad r \in [0, c_{\rho^*} + \log n],$$

where $\gamma(a_{\rho^*}, b_{\rho^*}c_{\rho^*} + b_{\rho^*}\log n) := \int_0^{b_{\rho^*}c_{\rho^*}+b_{\rho^*}\log n} r^{a_{\rho^*}-1}e^{-r}dr$ is positive and bounded above by $\Gamma(a_{\rho^*})$ for all $n \in \mathbb{N}$. This leads to a conjugate full conditional distribution on ρ^*, cf. Section 2.4, and also implies a bound on the sup-norm of ρ, used in the theoretical analysis, cf. the discussion after Theorem B.1 in the Supplement. Next, we model w via a family of centered Gaussian processes $W_\ell := \{W_\ell(z),\ z \in \mathcal{Z}\}$ with Automatic Relevance Determination (ARD) kernel,

$$\mathrm{E}[W_\ell(z)W_\ell(z')] = e^{-\sum_{j=1}^d \ell_j(z_j - z_j')^2}, \qquad z = (z_1, \dots, z_d),\ z' = (z_1', \dots, z_d'), \tag{4}$$

where $\ell_1, \dots, \ell_d > 0$ are length-scale hyper-parameters and $\ell = (\ell_1, \dots, \ell_d)$. This covariance function represents the anisotropic generalization of the standard square-exponential kernel, which prescribes $\ell_j = \ell_h$ for all $h, j = 1, \dots, d$. It offers desirable modeling flexibility in the present setting, where distinct covariates may have diverse physical nature and vary over vastly different ranges, possibly resulting in intensities with distinct smoothness levels along different directions. The ARD kernel is widely used in machine learning in such situations, e.g. (Rasmussen & Williams 2005, Chapter 5.1), and was shown by Bhattacharya et al. (2014), in simpler statistical models, to lead to optimal reconstruction of anisotropic functions.

We conclude the specification of Π_W (and of Π) by randomizing the length-scales in (4) as follows: We first draw $\theta_1, \dots, \theta_d \overset{\text{iid}}{\sim} \text{Beta}(a_\theta, b_\theta)$ for some $a_\theta, b_\theta > 0$. Then, for each $j = 1, \dots, d$, given θ_j, we set $\ell_j = \gamma_j^{\theta_j/d}$, where $\gamma_1, \dots, \gamma_d \overset{\text{iid}}{\sim} \Gamma(a_\gamma, b_\gamma)$ for some $a_\gamma, b_\gamma > 0$. In other words, each ℓ_j is independently modeled as a stochastic power of a gamma random variable. This construction is inspired by the hyper-prior from (Bhattacharya et al. 2014, Section 3.1), and is crucially used in the proof of our main result, Theorem 2.3 below, where the employed random exponentiation lends some additional flexibility to the hyper-prior, while also leading to a tight control over its complexity, similar to the findings from Bhattacharya et al. (2014). We note that $\ell_1, \dots, \ell_d$ are independent under our hyper-prior, resulting in a slight simplification of and an arguably more natural model than the construction in the latter reference, where the stochastic exponents are jointly drawn from a Dirichlet distribution.

In the specification of Π, the parameters $a_{\rho^*}, b_{\rho^*}, c_{\rho^*}, a_\theta, b_\theta, a_\gamma, b_\gamma$ are arbitrary positive quantities. In fact, they play no role in our proofs (only possibly affecting the constants pre-multiplying the rates), and we have also found them to be largely uninfluential in our empirical results, where they have been set to generically uninformative values. For example, for the simulation studies of Section 3, we have assigned $\theta_1, \dots, \theta_d \overset{\text{iid}}{\sim} \text{Beta}(2, 2)$.

Following the Bayesian paradigm, given data $D^{(n)}$ arising as described at the beginning of Section 2, and Π as above, the posterior distribution $\Pi(\cdot|D^{(n)})$ is given by the conditional distribution of $\rho|D^{(n)}$. By Bayes' theorem (e.g. (Ghosal & Van der Vaart 2017, p. 7)),

$$\Pi(A|D^{(n)}) = \frac{\int_A L^{(n)}(\rho)d\Pi(\rho)}{\int_{\mathcal{R}} L^{(n)}(\rho)d\Pi(\rho)}, \qquad A \subseteq \mathcal{R} \text{ measurable}, \tag{5}$$

where $L^{(n)}$ is the likelihood from (2), and where $\mathcal{R}$ is the collection of all measurable, bounded and nonnegative-valued functions defined on the covariate space $\mathcal{Z}$.

Remark 2.2 (Bounded covariate spaces)**.** *The assumption that $\mathcal{Z}$ be bounded is a convenient working assumption that entails no loss of generality since, if it were unbounded, we might 'pre-process' the covariates via a smooth and bijective map $\Phi : \mathbb{R}^d \to \mathbb{R}^d$ with bounded range, setting $\tilde{Z}^{(i)}(x) := \Phi(Z^{(i)}(x))$, $x \in \mathcal{W}$, $i = 1, \dots, n$. We would then proceed in the statistical analysis using the transformed covariates in place of the original ones, and then translate the obtained estimates back onto $\mathcal{Z}$ via the inverse map Φ^{-1}. A standard choice is given by*

$$\Phi(z) = (\phi(z_1), \dots, \phi(z_d)), \qquad z = (z_1, \dots, z_d) \in \mathcal{Z}, \tag{6}$$

where $\phi : \mathbb{R} \to [0, 1]$ is a smooth cumulative distribution function (c.d.f.), in which case $\tilde{Z}^{(i)}(x)$ takes values in $[0, 1]^d$. Analogous standardization steps are common practice in spatial statistics applications, for example being embedded within the popular `R` *package* `spatstat` *(Baddeley et al. (2016)) for kernel-based intensity estimation; see also (Guan 2008, Section 3.2.1).*

2.2 Adaptive anisotropic posterior contraction rates

We present our main theoretical results concerning the asymptotic behavior of the posterior distribution (5) as $n \to \infty$, under the paradigm of the 'frequentist analysis of Bayesian procedures' (e.g. Ghosal & Van der Vaart (2017)). We assume observations $D^{(n)} \sim P^{(n)}_{\rho_0}$ generated by some fixed (possibly anisotropic) ground truth ρ_0, and study the convergence of $\Pi(\cdot|D^{(n)})$ towards ρ_0. In the following result, we quantify the speed of such concentration with respect to the distance

$$d_Z(\rho_1, \rho_2) := \sqrt{\mathrm{E}\left\|\sqrt{\lambda_{\rho_1}} - \sqrt{\lambda_{\rho_2}}\right\|^2_{L^2(\mathcal{W})}} = \sqrt{\mathrm{E}\int_{\mathcal{W}} \left(\sqrt{\rho_1(Z((x))} - \sqrt{\rho_2(Z(x))}\right)^2 dx}, \tag{7}$$

where the expectation is with respect to the law of Z. This is a natural metric for the problem at hand, as it turns out to be closely related to the Hellinger distance between the observational densities (2), cf. Section B.3 in the Supplement. In the important case where Z is assumed to be stationary, d_Z can be shown to be equivalent to a standard L^2-type metric, under which the obtained rates coincide with the optimal ones, up to a logarithmic factor. See Section 2.3 below.

Theorem 2.3. *For $\alpha = (\alpha_1, \dots, \alpha_d) \in (0, \infty)^d$, let $\rho_0 \in C^\alpha(\mathcal{Z})$ satisfy $\inf_{z \in \mathcal{Z}} \rho_0(z) > 0$, and consider data $D^{(n)} \sim P^{(n)}_{\rho_0}$ arising as described at the beginning of Section 2. Let Π be a prior for ρ constructed as in Section 2.1, and let $\Pi(\cdot|D^{(n)})$ be the resulting posterior distribution. Then,*

$$\Pi\left(\rho : d_Z(\rho, \rho_0) > L n^{-\alpha_0/(2\alpha_0+1)} \log^C n \middle| D^{(n)}\right) \to 0, \qquad \alpha_0 = 1/\sum_{j=1}^{d} \alpha_j^{-1},$$

in $P^{(\infty)}_{\rho_0}$-probability as $n \to \infty$, for all sufficiently large $L > 0$ and some large enough $C > 0$.

The proof of Theorem 2.3 is given in the supplementary Section A. The result holds for a slightly more general prior class, fully described in Condition A.1 therein.

Theorem 2.3 asserts that if $\rho_0 \in C^{\alpha}(\mathcal{Z})$, then, with probability tending to one, any posterior sample $\rho \sim \Pi(\cdot|D^{(n)})$ is within a small d_Z-neighborhood of ρ_0 with radius shrinking (nearly) at the order $n^{-\alpha_0/(2\alpha_0+1)}$. The quantity α_0 is called 'effective smoothness' (Hoffman & Lepski 2002, p. 326), and is known to characterize the minimax optimal rates of estimation over anisotropic function spaces; see e.g. Nyssbaum (1987) for results in nonparametric regression. We note that α_0 is increasing with respect to each component of the vector of regularities α; in particular, the sequence $n^{-\alpha_0/(2\alpha_0+1)}$ can be made arbitrarily close to the parametric rate $n^{-1/2}$ if ρ_0 is infinitely differentiable along each direction. Since the considered prior Π requires no information about α (or α_0) for its construction, we conclude that it is able to automatically 'adapt' to the (possibly) anisotropic smoothness. This is in line with the findings from (Bhattacharya et al. 2014, Section 3.1), which we build on to investigate the present covariate-based intensity estimation problem.

In the isotropic case where $\alpha_j = a$ for some $a > 0$ and all $j = 1, \dots, d$, we have $\alpha_0 = a/d$, and Theorem 2.3 recovers the usual nonparametric rate $n^{-a/(2a+d)}$, up to a logarithmic factor. On the other hand, in the presence of a genuine anisotropy, since $\alpha_0 \geq \min_{j=1,\dots,d} \alpha_j/d$, treating ρ_0 as having isotropic smoothness generally results in slower rates, with greater loss of efficiency in higher dimensions. Thus, multi-bandwidth Gaussian process priors are suited to both scenarios, while it was shown by (Bhattacharya et al. 2014, Section 3.5) that single-bandwidth procedures lead to a sub-optimal performance if the ground truth is anisotropic.

Remark 2.4 (Bounded away from zero intensities)**.** *The proof of Theorem 2.3 requires that ρ_0 be bounded away from zero. This condition similarly underpins previous results for nonparametric Bayesian intensity estimation (in non-covariate-based models), e.g. Gugushvili & Spreij (2013), Belitser et al. (2015), Kirichenko & van Zanten (2015). However, this imposes little restriction in practice since, reasoning similarly to the discussion after Theorem 1 in Belitser et al. (2015), if ρ_0 were not (or not known to be) bounded away from zero, we might modify the observed point patterns $\{N^{(i)}\}_{i=1}^n$ by adding independently sampled standard Poisson processes. The law of the resulting data would then be characterized by a covariate-based intensity equal to $1 + \rho_0$, which is bounded below by one and has the same smoothness properties as ρ_0. Using this, the above multi-bandwidth Gaussian process methods could be used to make inference on the function $1 + \rho_0$ (and therefore also on ρ_0), with strict theoretical guarantees provided by Theorem 2.3.*

Remark 2.5 (Deterministic covariates)**.** *Our approach readily allows for the case where both random and deterministic covariates are of interest, say $Z_{rand} := \{Z_{rand}(x),\ x \in \mathcal{W}\}$ and $Z_{det} := \{Z_{det}(x),\ x \in \mathcal{W}\}$, respectively. Letting $Z(x) := (Z_{rand}(x), Z_{det}(x))$ and considering observations $Z^{(i)}(x) := (Z^{(i)}_{rand}(x), Z_{det}(x))$, $i = 1, \dots, n$, where $Z^{(1)}_{rand}, \dots, Z^{(n)}_{rand}$ are i.i.d. copies of Z_{rand}, the posterior distribution is again given by (5), and can be approximately sampled from via the MCMC algorithm from Section 2.4 below. Furthermore, inspection of the proof of Theorem 2.3 shows that its conclusion remains valid in this setting, with the distance d_Z from (7) now equaling*

$$d_Z^2(\rho_1, \rho_2) = \mathrm{E} \int_{\mathcal{W}} \left(\sqrt{\rho_1(Z_{rand}(x), Z_{det}(x))} - \sqrt{\rho_2(Z_{rand}(x), Z_{det}(x))} \right)^2 dx,$$

with the expectation being with respect to the law of Z_{rand}. Among the others, this allows to study purely spatial effects on the intensity by taking $Z_{det}(x) = x$. See Section C.3 in the Supplement for an illustration of this with synthetic data.

Remark 2.6 (Discrete covariates)**.** *As our primary focus is on Gaussian process methods for covariate-based intensities, we do not consider in details the case of discrete* *covariates, as these would require completely different priors. However, we note that our general concentration result, Theorem B.1 in the Supplement, imposes no restrictions on $\mathcal{Z}$, and thus can be used to study the performance of Bayesian procedures in this setting as well. In particular, arguing similarly to the proof of Proposition 3.20 in Giordano et al. (2025) would lead to near-parametric posterior contraction rates under mild conditions on the prior distribution. Combining this with the results derived in the present article, mixed scenarios with both continuous and discrete covariates could be further investigated. We do not pursue such extensions here for the sake of conciseness.*

2.3 Posterior contraction rates in the case of stationary covariates

Stationarity is a common assumption for the analysis of spatially correlated data, e.g. Cressie (2015). In the present setting, stationarity of the covariates entails the often realistic scenario, which can be tested (e.g. Bandyopadhyay & Subba Rao (2017)), where the marginal distribution of the random field Z is homogeneous across the observation window, namely that $Z(x) \sim \nu_Z$ for each $x \in \mathcal{W}$, for some probability measure ν_Z supported on $\mathcal{Z}$.

For stationary covariates, the metric d_Z appearing in Theorem 2.3 can be made more explicit. Indeed, an application of Fubini's theorem yields, for all $\rho_1, \rho_2 \in \mathcal{R}$,

$$\begin{aligned} d_Z^2(\rho_1, \rho_2) &= \int_{\mathcal{W}} \mathrm{E}\left(\sqrt{\rho_1(Z((x))} - \sqrt{\rho_2(Z(x))}\right)^2 dx \\ &= \int_{\mathcal{W}} \int_{\mathcal{Z}} \left(\sqrt{\rho_1(z)} - \sqrt{\rho_2(z)}\right)^2 d\nu_Z(z) dx = \mathrm{vol}(\mathcal{W}) \|\rho_1 - \rho_2\|^2_{L^2(\mathcal{Z}, \nu_Z)}. \end{aligned}$$

Further, if ν_Z is absolutely continuous with bounded and bounded away from zero p.d.f., we have $\|\rho_1 - \rho_2\|_{L^2(\mathcal{Z},\nu_Z)} \simeq \|\rho_1 - \rho_2\|_{L^2(\mathcal{Z})}$, implying that d_Z is equivalent to the standard $L^2(\mathcal{Z})$-metric. For example, this is the case if the stationary distribution ν_Z is known, and if we pre-process the observed covariates $\{Z^{(i)}\}_{i=1}^n$ as described in Remark 2.2 via the c.d.f. associated to ν_Z, yielding a uniform stationary distribution. When ν_Z is not known, a pre-processing step involving the empirical c.d.f. of the covariates is often used in practice, e.g. Baddeley et al. (2012).

Under the latter assumptions on Z, the conclusion of Theorem 2.3 can be written as

$$\Pi\left(\rho : \|\rho - \rho_0\|_{L^2(\mathcal{Z})} > L n^{-\alpha_0/(2\alpha_0+1)} \log^C n \middle| D^{(n)}\right) \to 0,$$

in $P_{\rho_0}^{(\infty)}$-probability as $n \to \infty$, holding for all sufficiently large $L, C > 0$. The rate $n^{-\alpha_0/(2\alpha_0+1)}$ is known to be minimax optimal, in various statistical models, for estimating in L^2-risk functions with anisotropic Hölder regularity equal to α, including in nonparametric regression (e.g. Nyssbaum (1987)) and density estimation (e.g. Barron et al. (1999)). Following the strategy for deriving lower bounds in intensity estimation problems laid out in (Kutoyants 1998, Chapter 6.2), this conclusion can be extended to the present setting as well, showing that the proposed methods adaptively achieve optimal posterior contraction rates in the case of stationary covariates.

2.4 Posterior sampling via a Metropolis-within-Gibbs algorithm

Noting that the posterior distribution from (5) is not available in closed form, we construct a suitable MCMC algorithm of Metropolis-within-Gibbs type to approximately draw from $\Pi(\cdot|D^{(n)})$. Following the usual MCMC methodology, we then employ the generated samples to concretely compute Bayesian point estimates and credible sets.

A delicate aspect for likelihood-based nonparametric procedures for inhomogeneous point processes is the analytical intractability of the likelihood, since the latter involves an integral of the intensity over the observation window, cf. (2), which cannot generally be computed in closed form. In our implementation, we tackle this difficulty resorting to numerical integration, specifically via piece-wise constant quadrature. In the context of nonparametric Bayesian intensity estimation for models without covariates, more sophisticated methods based on data augmentation have been proposed to handle the resulting 'doubly-intractable' posteriors; see Adams et al. (2009). These techniques could conceivably be adapted to the present covariate-based setting; however, we did not pursue such extensions here, as we found our approach to yield satisfactory results both in the simulation studies of Section 3 and in the data analysis of Section 4. Devising 'exact' MCMC samplers for the problem at hand, and comparing their performance to our approach based on numerical likelihood approximations, is an interesting direction for future work.

The employed MCMC algorithm alternates samples from the full conditional distributions, given below, of the quantities $\rho^*, \theta_1, \dots, \theta_d, \ell_1, \dots, \ell_d$ and w, cf. Section 2.1. For the functional parameter $w : \mathcal{Z} \to \mathbb{R}$, we introduce the 'high-dimensional' discretization

$$w(z) = \sum_{v=1}^{V} w_v \psi_v(z), \qquad V \in \mathbb{N}, \qquad w_1, \dots, w_V \in \mathbb{R}, \qquad z \in \mathcal{Z}, \tag{8}$$

where $\psi_1, \dots, \psi_V$ are linear interpolation functions associated to a pre-determined grid $z_1, \dots, z_V \in \mathcal{Z}$, sufficiently refined as to guarantee that the numerical interpolation error is negligible compared to the statistical one. Under the discretization (8), we have $w(z_v) = w_v$ for all $v = 1, \dots, V$, and for any $z \in \mathcal{Z}$, the value $w(z)$ is found by linearly interpolating the pairs $\{(z_v, w_v)\}_{v=1}^V$. Accordingly, we identify w with the vector $(w_1, \dots, w_V)$, which under Π, conditionally on $\ell = (\ell_1, \dots, \ell_d)$, is assigned the centered multivariate Gaussian prior

$$w \sim N_V(0, C_\ell), \qquad (C_\ell)_{v,v'} = e^{-\sum_{j=1}^d \ell_j (z_{v,j} - z_{v',j})^2}, \qquad v, v' = 1, \dots, V. \tag{9}$$

Starting from some initialization (which we set to a cold start), and given the current draws for all the parameters, each step of the Metropolis-within-Gibbs algorithm alternates samples from:

1. The full conditional distribution of the upper bound ρ^* of the intensity,

$$\begin{aligned}\Pi(\tilde{\rho}^* | D^{(n)}, \theta_1, \dots, &\theta_d, \ell_1, \dots, \ell_d, w)\\ &\propto \Pi_{\rho^*}(\tilde{\rho}^*) \prod_{i=1}^n e^{\sum_{k=1}^{K^{(i)}} \log(\tilde{\rho}^* \sigma(w(Z^{(i)}(X_k^{(i)})))) - \int_{\mathcal{W}} \tilde{\rho}^* \sigma(w(Z^{(i)}(x)))dx}\\ &\propto \Pi_{\rho^*}(\tilde{\rho}^*)(\tilde{\rho}^*)^{\sum_{i=1}^n K^{(i)}} e^{-\tilde{\rho}^* \int_{\mathcal{W}} \sum_{i=1}^n \sigma(w(Z^{(i)}(x)))dx},\end{aligned}$$

   which, recalling that Π_{ρ^*} is a truncated $\Gamma(a_{\rho^*}, b_{\rho^*})$ distribution over $[0, c_{\rho^*} + \log n]$, is again truncated gamma with updated parameters $a_{\rho^*} + \sum_{i=1}^n K^{(i)}$ and $b_{\rho^*} + \int_{\mathcal{W}} \sum_{i=1}^n \sigma(w(Z^{(i)}(x)))dx$. The latter is efficiently computed in practice via quadrature.

2. The full conditional distributions of each length-scale exponent θ_j, $j = 1, \dots, d$,

$$\Pi(\tilde{\theta}_j | D^{(n)}, \rho^*, \theta_1, \dots, \theta_{j-1}, \theta_{j+1}, \dots, \theta_d, \ell_1, \dots, \ell_d, w) \propto \ell_j^{a_\gamma \frac{d}{\tilde{\theta}_j}} e^{-b_\gamma \ell_j^{d/\tilde{\theta}_j}} \tilde{\theta}_j^{a_\theta - 2} (1 - \tilde{\theta}_j)^{b_\theta - 1}, \tag{10}$$

having used that, a priori, $\theta_j \overset{\text{iid}}{\sim} \text{Beta}(a_\theta, b_\theta)$ and that, given θ_j, $\ell_j = \gamma_j^{\theta_j/d}$ with $\gamma_j \overset{\text{iid}}{\sim} \Gamma(a_\gamma, b_\gamma)$. Sampling from the above is achieved via a Metropolis-Hastings MCMC algorithm with proposal distribution equal to the beta hyper-prior, whose acceptance probabilities are analytically computed from (10). Note that, since the full conditional distributions are independent, the updates of $\theta_1, \dots, \theta_d$ can be performed in parallel.

3. The full conditional distribution of each length-scale ℓ_j, $j = 1, \dots, d$,

$$\begin{aligned}\Pi(\tilde{\ell}_j|D^{(n)}, \rho^*, \theta_1, \dots, &\theta_d, \ell_1, \dots, \ell_{j-1}, \ell_{j+1}, \dots, \ell_d, w) \\ &\propto \det{}^{-1/2}(C_{\tilde{\ell}}) e^{-\frac{1}{2} w^T (C_{\tilde{\ell}})^{-1} w} \tilde{\ell}_j^{a_\gamma d/\theta_j - 1} e^{-b_\gamma \tilde{\ell}_j^{d/\theta_j}},\end{aligned} \tag{11}$$

where $\tilde{\ell} := (\ell_1, \dots, \ell_{j-1}, \tilde{\ell}_j, \ell_{j+1}, \dots, \ell_d)$. Above, we have again exploited the product structure of the hyper-prior. Further, we have used the fact that, under the discretization (8), conditionally on $\tilde{\ell}$, $w \sim N(0, C_{\tilde{\ell}})$ with $C_{\tilde{\ell}}$ as in (9). Sampling from (11) is achieved via the adaptive random walk Metropolis-Hasting algorithm (Haario et al. (2001)). This can also be parallelized.

4. The full conditional distribution of the high-dimensional parameter w,

$$\Pi(\tilde{w}|D^{(n)}, \rho^*, \theta_1, \dots, \theta_d, \ell_1, \dots, \ell_d) \propto L^{(n)}(\rho^* \sigma \circ \tilde{w}) \det{}^{-1/2}(C_\ell) e^{-\frac{1}{2} \tilde{w}^T (C_\ell)^{-1} \tilde{w}}, \tag{12}$$

where $L^{(n)}$ is the likelihood from (2), and where we have used the notation

$$(\rho^* \sigma \circ \tilde{w})(z) = \rho^* \sigma\Big(\sum_{v=1}^{V} \tilde{w}_v \psi_v(z)\Big), \qquad \tilde{w}_1, \dots, \tilde{w}_V \in \mathbb{R}, \qquad z \in \mathcal{Z}.$$

We extract approximate samples from (12) via the ‘pre-conditioned Crank-Nicholson’ (pCN) algorithm, which is a dimension-robust Metropolis-Hastings MCMC sampling method, specifically designed for procedures based on Gaussian priors, commonly used in inverse problems and data assimilation; see Cotter et al. (2013). This generates an $\mathbb{R}^V$-valued Markov chain $\{\omega_u,\ u \in \mathbb{N}\}$ through the repetition of the following two operations:

- Draw a sample from the prior $\xi \sim N_V(0, C_{\tilde{\ell}})$ and construct the proposal $\omega := \sqrt{1 - 2\zeta}\omega_{u-1} + \sqrt{2\zeta}\xi$, where $\zeta \in (0, 1/2)$ is a fixed step-size.
- Define the new element in the pCN chain by

$$\omega_u := \begin{cases} \omega, & \text{with probability } 1 \wedge \frac{L^{(n)}(\rho^* \sigma \circ \omega)}{L^{(n)}(\rho^* \sigma \circ \omega_{u-1})}, \\ \omega_{u-1}, & \text{otherwise.} \end{cases}$$

The first step is straightforward, as well as relatively inexpensive even for moderately high discretization dimensions V. The second necessitates the evaluation of the proposal likelihood, which we again tackle by quadrature. The resulting Markov chain can be shown to be reversible and to have stationary measure equal to the full conditional distribution (12), e.g. (Nickl 2023, Proposition 1.2.2). Further, the pCN acceptance probabilities are known to be stable with respect to the discretization dimension, Cotter et al. (2013), implying desirable mixing properties for statistical applications with functional unknowns, Hairer et al. (2014).

3 Simulation studies

We assess our approach in extensive numerical simulations. We take the centered unit square $\mathcal{W} = [-1/2, 1/2]^2$ as the observation window, fix the ground truth ρ_0 and, for $i = 1, \dots, n$, draw an independent realization $Z^{(i)}$ of a d-variate random field Z, conditionally on which we sample the point pattern $N^{(i)}$. We then implement posterior inference via the MCMC algorithm described in Section 2.4. All experiments were carried out in `R` on an Intel(R) Core(TM) i7-10875H 2.30GHz processor with 32 GB of RAM. Numerical integration over the window $[-1/2, 1/2]^2$ is performed via piece-wise constant quadrature using a uniform square grid with 2500 nodes.

We compare the obtained results to the performance of an alternative kernel-type method, which is the standard approach in spatial statistics; see e.g. the monograph Baddeley et al. (2016). To our knowledge, the existing frequentist literature on covariate-based intensity estimation is largely focused on the setting where a single observation of the covariates and points are available (possibly over a large domain or under an increasing intensity assumption), e.g. Guan (2008), Baddeley et al. (2012), Borrajo et al. (2020). There appears to be no definite consensus on how to tackle the joint investigation of repeated observations, despite interest in this case having been raised since at least Diggle et al. (1991). An overview of possible aggregation strategies was presented by (Illian et al. 2008, Chapter 4). Following the latter, we consider a simple average of individual covariate-based kernel intensity estimators,

$$\hat{\rho}_\kappa(z) = \frac{1}{n} \sum_{i=1}^{n} \hat{\rho}_\kappa^{(i)}(z), \qquad z \in \mathcal{Z}, \tag{13}$$

where each $\rho_\kappa^{(i)}$ is defined according to the 'ratio-form' from Baddeley et al. (2012),

$$\hat{\rho}_\kappa^{(i)}(z) = \frac{1}{g^{(i)}(z)} \sum_{k=1}^{K^{(i)}} \kappa(Z^{(i)}(X_k^{(i)}) - z), \qquad z \in \mathcal{Z}. \tag{14}$$

Above, κ is a d-dimensional smoothing kernel and $g^{(i)}$ is the (non-normalized) density of the empirical spatial c.d.f. of $Z^{(i)}$. See (Baddeley et al. 2012, Section 3) for details, and also Guan (2008) and Borrajo et al. (2020) for similar procedures. In the experiments, we concretely compute $\hat{\rho}_\kappa$ using the built-in implementation included in the popular `R` package `spatstat` (Baddeley et al. (2016)), opting for the default settings under which κ is Gaussian and the bandwidth is selected according to Silverman's rule-of-thumb, Silverman (1986).

3.1 Results for univariate covariates

We start with a one-dimensional scenario, taking Z as a (centered) square-exponential process with length-scale equal to 0.005, transformed via the standard normal c.d.f. as described in Remark 2.2. With this choice, Z is supported on $\mathcal{Z} = [0, 1]$, is stationary, and has invariant measure equal to the uniform distribution on $[0, 1]$, falling within the framework of Section 2.3. The ground truth is set to be proportional to the restriction on $[0, 1]$ of a univariate skew normal p.d.f.,

$$\rho_0(z) = 5 f_{SN}(z; 0.8, 0.3, -5), \qquad z \in [0, 1], \tag{15}$$

cf. Figure 2 below. This results in point patterns concentrated around the regions with covariate value near 0.65; see Figure 1. The expected number of points per observation is (slightly smaller than) 5. Independent samples from Z are drawn via a discretization scheme similar to (8). The realizations of the point pattern are obtained via the 'thinning' procedure described in (Adams et al. 2009, Section 2.3), which is included in the `R` package `spatstat` (Baddeley et al. (2016)).

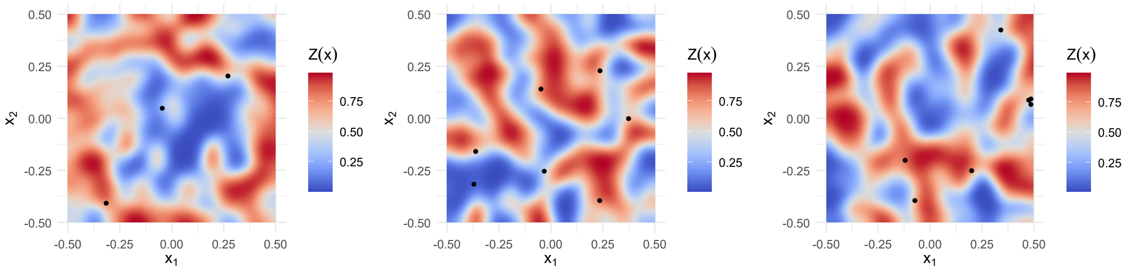

Figure 1: Independent realizations of the covariates and the point pattern with intensity (15).

Figure 2 displays the posterior mean $\hat{\rho}_{\Pi}^{(n)} := E^{\Pi}[\rho|D^{(n)}]$ for $n = 250, 500, 1000$, alongside associated point-wise 95%-credible intervals. As expected from Theorem 2.3, the posterior appears to concentrate around ρ_0 as the number of observations increases. For visual comparison, we also include the averaged kernel estimate $\hat{\rho}_{\kappa}$ from (13). Table 1 reports the (numerically approximated) L^2-estimation errors, averaged across 100 replications of each experiment. The corresponding standard deviations and average relative estimation errors are also included. Except for the lowest sample size, at which $\hat{\rho}_{\Pi}^{(n)}$ and $\hat{\rho}_{\kappa}$ achieve similar results, the posterior mean is seen to achieve lower estimation errors than the kernel alternative, whose performance displays a plateau. This hints at a superior capability of the former to combine information across multiple realizations.

The posterior means and credible intervals were computed via the MCMC algorithm described in Section 2.4, choosing the pCN step-size ζ within the range $[0.01, 0.5]$, depending on the sample size, so to achieve stable acceptance probabilities of around 30%. The discretization scheme (8) for the functional parameter was based on $V = 200$ equally spaced nodes in $[0, 1]$. We initialized each run at a cold start, terminating it after 20000 iterations, with 5000 burn-in samples. Execution times ranged between 6 and 125 minutes. The 'hyper-hyper-parameters' of the prior were set to $\alpha_{\rho^*} = 1$, $b_{\rho^*} = 2$, $c_{\rho^*} = 25$, $a_\theta = b_\theta = 2$ and $\alpha_\gamma = b_\gamma = 1$.

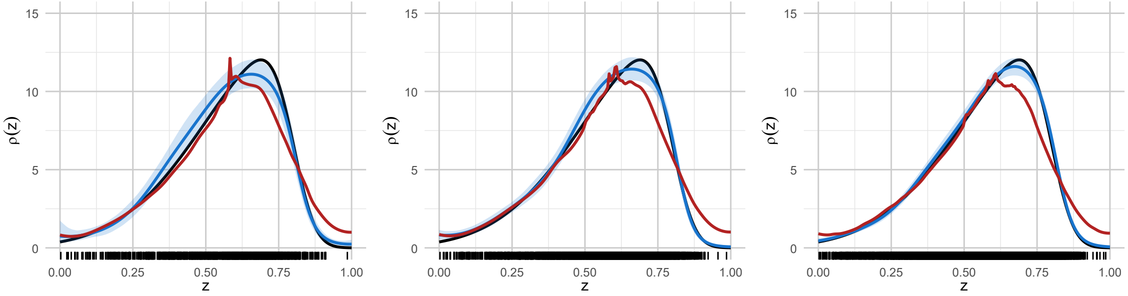

Figure 2: Left to right: Posterior means (solid blue), pointwise 95%-credible intervals (shaded blue) and averaged kernel estimates (solid red) for $n = 250, 500, 1000$. The ground truth ρ_0 from (15) is shown in solid black in each plot for comparison.

n	50	250	500	1000
$\|\hat{\rho}_\Pi^{(n)} - \rho_0\|_{L^2}$	1.25 (0.32)	0.55 (0.09)	0.43 (0.07)	0.35 (0.05)
$\|\hat{\rho}_\Pi^{(n)} - \rho_0\|_{L^2}/\|\rho_0\|_{L^2}$	0.19 (0.05)	0.09 (0.01)	0.07 (0.01)	0.05 (0.008)
$\|\hat{\rho}_\kappa - \rho_0\|_{L^2}$	1.18 (0.30)	0.96 (0.12)	0.93 (0.08)	0.94 (0.06)
$\|\hat{\rho}_\kappa - \rho_0\|_{L^2}/\|\rho_0\|_{L^2}$	0.18 (0.05)	0.15 (0.02)	0.14 (0.01)	0.14 (0.005)

Table 1: Average L^2-estimation errors (and their standard deviations) over 100 repeated experiments for the posterior mean $\hat{\rho}_\Pi^{(n)}$ and the averaged kernel estimate $\hat{\rho}_\kappa$.

3.2 Results for bivariate covariates

To simulate bi-dimensional covariates $Z(x) = (Z_1(x), Z_2(x))$, we take $Z_1 := \{Z_1(x),\ x \in \mathcal{W}\}$ as in the above univariate experiment, and set $Z_2 := \{Z_2(x),\ x \in \mathcal{W}\}$ equal to an independent square-exponential process with larger length-scale 0.05, again under the standard normal c.d.f. transformation. See Figure 11 in the Supplement below for a visual comparison of Z_1 and Z_2. We construct the ground truth via a linear combination of two bi-dimensional normal p.d.f.'s,

$$\rho_0(z_1, z_2) = \max\{0, 10 - 10 f_N(z_1, z_2; (0.8, 0.3), \Sigma) + 10 f_N(z_1, z_2; (0.3, 0.8), \Sigma)\}, \quad (16)$$

for $(z_1, z_2) \in [0,1]^2$, where $\Sigma = \mathrm{diag}(0.08^2, 0.5^2)$. The resulting true intensity is anisotropic, with noticeably smaller characteristic length-scales in the first argument, cf. Figure 3.

The results for the bi-dimensional scenario are summarized in Figure 3 and Table 2. The first three panels show the posterior mean for increasing sample sizes $n = 50, 250, 1000$, displaying again a clear improvement in the visual agreement with the ground truth (depicted in the last panel). Table 2 reports the absolute and relative L^2-estimation errors for the posterior mean and the kernel procedure, averaged over 100 replicated experiments. In line with the previous results, we observe a steady decay in the estimation errors associated to the posterior mean, whose performance is overall superior to the one of the averaged kernel estimator. For the computation of the posterior mean, we employed a discretization of the parameter space with $V = 600$ linear interpolation functions, based on a triangular tessellation of the covariate space $[0,1]^2$ with maximal element area equal to 0.0014. All the other parameters in the prior specification and the implementation of the MCMC algorithm were left unchanged from the one-dimensional experiments. Running times ranged between 15 and 260 minutes.

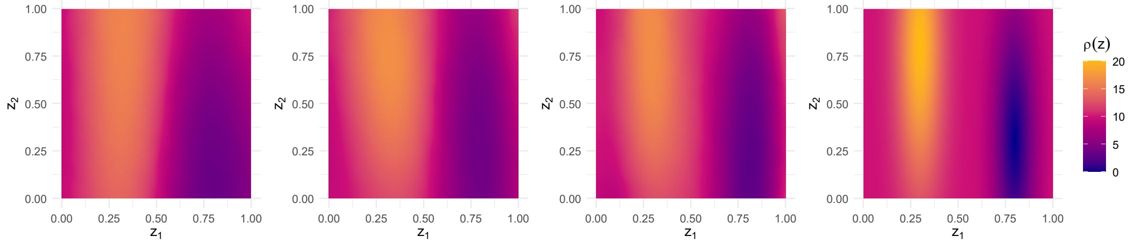

Figure 3: Left to right: Posterior means for $n = 50, 250, 1000$ and the anisotropic ground truth (16).

n	10	50	250	1000
$\|\hat{\rho}_\Pi^{(n)} - \rho_0\|_{L^2}$	3.58 (0.48)	2.54 (0.49)	1.95 (0.5)	1.41 (0.21)
$\|\hat{\rho}_\Pi^{(n)} - \rho_0\|_{L^2}/\|\rho_0\|_{L^2}$	0.33 (0.04)	0.24 (0.05)	0.18 (0.05)	0.13 (0.02)
$\|\hat{\rho}_\kappa - \rho_0\|_{L^2}$	3.37 (0.42)	2.31 (0.23)	2.05 (0.06)	1.99 (0.03)
$\|\hat{\rho}_\kappa - \rho_0\|_{L^2}/\|\rho_0\|_{L^2}$	0.31 (0.04)	0.21 (0.02)	0.19 (0.01)	0.18 (0.004)

Table 2: Average L^2-estimation errors and their standard deviations over 100 repeated experiments for the posterior mean $\hat{\rho}_\Pi^{(n)}$ and the averaged kernel estimate $\hat{\rho}_\kappa$.

Further details on the simulations studies, including diagnostic plots for the MCMC algorithm can be found in Section C of the Supplement. There, additional experiments with different ground truths, purely spatial effects and over-parametrized models are also provided.

4 Applications to a Canadian wildfire dataset

The study of the distribution of wildfires and of their relationship with geographical and environmental factors is well established in the spatial statistics community. Recent contributions were provided by Juan et al. (2012), Borrajo et al. (2020), Koh et al. (2023), among the others. The existing literature highlights that the spread of wildfires is heavily influenced by meteorological conditions such as high temperatures, prolonged dry periods, and moderate-to-strong winds.

In this section, we present an application to a Canadian wildfire dataset. Canada maintains an advanced wildfire monitoring system, and detailed daily data spanning the last two decades is publicly available at the Canadian Wildland Fire Information System website (http://cwfis.cfs.nrcan.gc.ca/home), comprising the geographical coordinates of the hotspots and complete environmental information. For our analysis, we extracted from this large dataset annual recordings from 2004 to 2022 of the locations of the wildfires over the month of June (which corresponds to the peak activity in Canada, cf. Borrajo et al. (2020)), alongside coordinate-wise monthly average temperatures, precipitation levels and wind speeds. We focused on a few selected provinces, specifically Ontario, in the eastern part of Canada, Saskatchewan, in the central region, and British

Columbia, on the Western coast. Here, we present the results for Ontario, deferring the rest of the analysis to Section D of the Supplement.

The Ontario dataset comprises $n = 19$ spatial point patterns $\{N^{(i)}\}_{i=2004}^{2022}$ representing the wildfire locations, cf. Figure 4, and the same number of tri-dimensional spatial covariate fields $\{Z^{(i)}\}_{i=2004}^{2022}$, where $Z^{(i)} = (Z_{\text{temp}}^{(i)}, Z_{\text{prec}}^{(i)}, Z_{\text{wind}}^{(i)})$. The data displays some strong variability, with the number of wildfires ranging from 2 (in June 2004) to 130 (in 2021), and with a wide spectrum of covariate values. Another distinctive characteristic is that the covariates exhibit fairly different behaviors: While the temperature fields mostly change smoothly over space, precipitations and winds tend to display more abrupt variations, possibly as a result of currents, orographic features and other environmental factors. The necessity to handle this heterogeneity provides the main motivation for the use of a multi-bandwidth method.

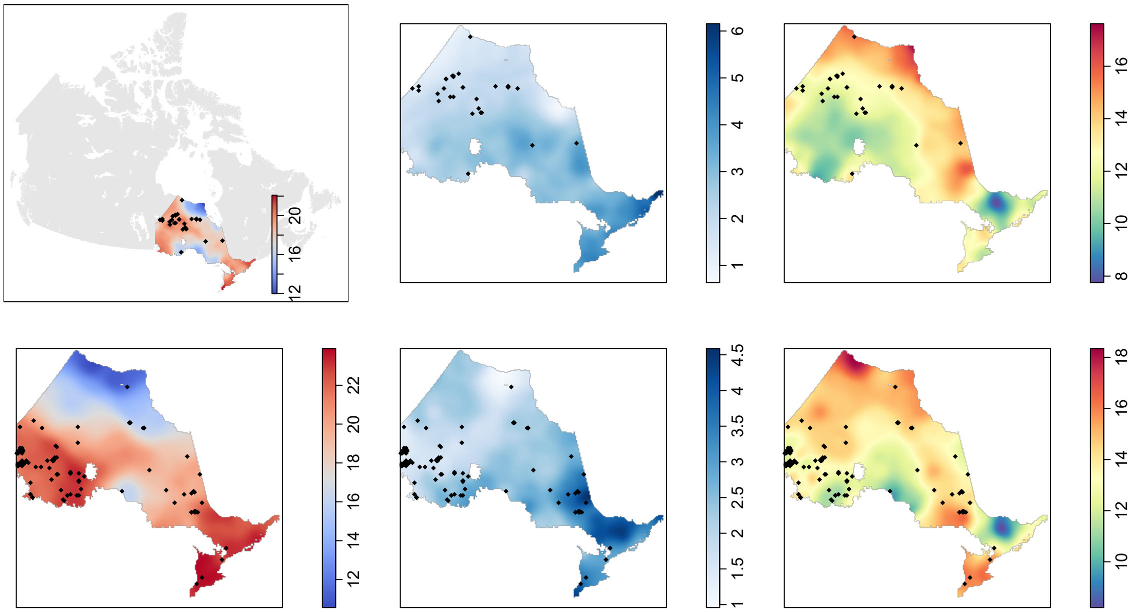

Figure 4: Top row, left to right: Average temperatures (in Celsius), precipitations (in mm/m^2) and wind speeds (in km/h) in Ontario during June 2013. Bottom row: Observations for 2021. The wildfires are represented by black dots (respectively, 34 and 130 in total).

4.1 Exploratory univariate analysis

For a preliminary analysis, the three panels of Figure 5 show the posterior means $\hat{\rho}_{\Pi,\text{temp}}, \hat{\rho}_{\Pi,\text{prec}}, \hat{\rho}_{\Pi,\text{wind}}$, respectively obtained using each covariate individually. The results capture, in line with the literature, a positive association between higher temperatures and increased risks of wildfires, with a sharp raise between 16°C and 25°C. A strong negative impact is inferred for the precipitation level, particularly above 1 mm/m^2, while windy conditions appear to increase the intensity only for some distinctive median speeds around 13 km/h. In Figure 5, we also include averaged kernel estimates constructed similarly to (13), with some structural modifications to better handle the variability exhibited by the number of observed wildfires and by the covariates across the years. Specifically, we restricted the individual ‘yearly’ kernel estimators (defined as in (14)) to their empirical support, and then considered a weighted average, with weights proportional to the number of events. The kernel-based estimates are in general agreement with the trends identified by the posterior means; however, despite the aforementioned corrections, they tend to exhibit a slightly more erratic behavior, being more heavily influenced by outlying contributions, and displaying some boundary effects.

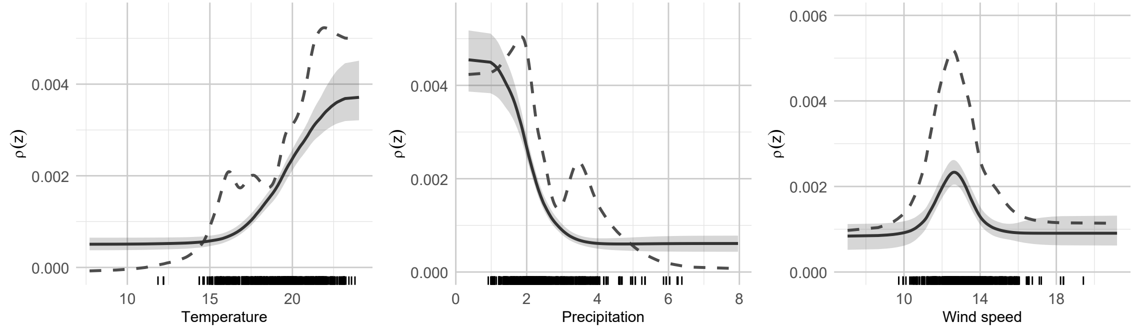

Figure 5: Left to right: Posterior means (solid line) and point-wise 95%-credible intervals (shaded region) for the wildfire intensity as a function of the average temperature, precipitation level and wind speed, respectively. The dashed lines show the kernel-based estimates.

In the analysis, the individual covariates were mapped onto the unit interval $[0, 1]$ as described in Remark 2.2 via the c.d.f. of the $N(0, 10)$ distribution, and then transformed back to the original scale for the display of the estimates in Figure 5 via an application of the inverse transformation. The parameters in the prior were chosen as $\alpha_{\rho^*} = 1$, $b_{\rho^*} = 2$, $c_{\rho^*} = 1$, $a_\theta = b_\theta = 2$ and $\alpha_\gamma = b_\gamma = 1$. $V = 200$ equally spaced nodes in $[0, 1]$ were used for the discretization (8) of the functional parameter. The runs of the sampler were iterated for 20000 steps, with burn-in times equal to 5000. Across the three scenarios, the same step-size $\zeta = 0.1$ for the pCN algorithm was used, yielding a stabilization of the acceptance probabilities between 20% and 30%.

Figure 6 displays the plug-in posterior means $\hat{\lambda}^{(i)}_{\rho,\text{temp}} := \hat{\rho}_{\Pi,\text{temp}} \circ Z^{(i)}_{\text{temp}}$ of the spatial intensity based on the location-specific average temperature, for some selected years $i = 2013, 2015, 2021$. We note that, while the estimate $\hat{\rho}_{\Pi,\text{temp}}$ is based on the combined information from 2004 to 2022, the yearly variability of the covariates results in different spatial intensity estimates which manage to capture year-specific trends, even in years with a relatively low number of events.

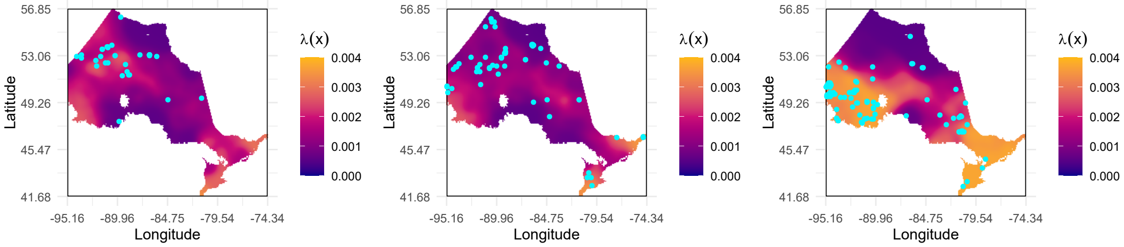

Figure 6: Left to right: Plug-in posterior means of the spatial intensity based on the average temperature, for the years $2013, 2015$ and 2021, respectively.

4.2 Full analysis

Next, we present the full analysis based on the joint information on temperatures, precipitations and winds. For ease of visualization, in Figure 7, we report two-dimensional 'marginal plots' of the obtained posterior means, resulting from fixing the value of the average wind speeds at the 0.05- and 0.95-quantiles (10.72 km/h and 16.21 km/h, respectively), and at the median (13.50 km/h). These reinforce the findings from the exploratory step, with the greatest intensities being associated to higher temperatures (above 19°C) and drier conditions (with average precipitations below 2 mm/m^2). Relatively high residual risks are also detected at extreme temperatures, despite heavy precipitations, or in correspondence of particularly dry weather. Concerning the influence of the wind, an interesting shift is captured at the median, where the overall risk is higher, in agreement with the effect shown in Figure 5 (right). We further note that the estimated intensity is generally lower at the 0.95-quantile, indicating a negative impact of very strong winds. Here, kernel-based estimates were not pursued, since the implementation in the `R` package `spatstat` (Baddeley et al. (2016)) that we used throughout the experiments does not readily handle more than two covariates. Figure 8 shows the corresponding spatial plug-in posterior means for the years 2013, 2015 and 2021. Compared to Figure 6, the three-dimensional model appears to be able to better reconstruct the structure of the point patterns across the years. This highlights the usefulness of employing joint meteorological information on temperatures, precipitations and winds in order to understand the distribution of wildfires.

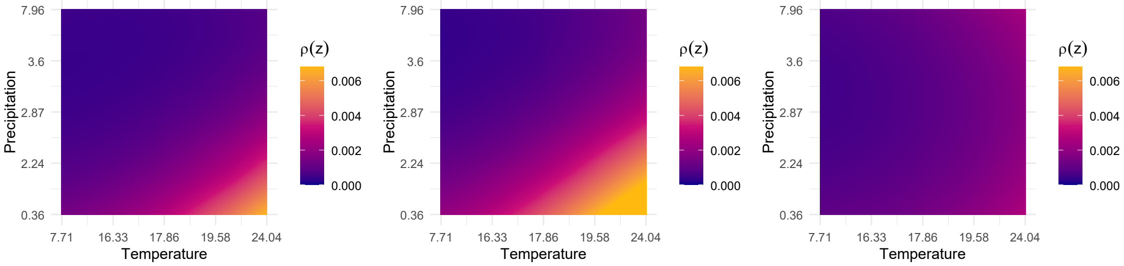

Figure 7: Left to right: 'Marginal' posterior means of the wildfire intensity as a function of the average temperature and precipitation level, at the .05 quantile (10.72 km/h), median (13.50 km/h) and .95 quantile (16.21 km/h) of the average wind speeds, respectively.

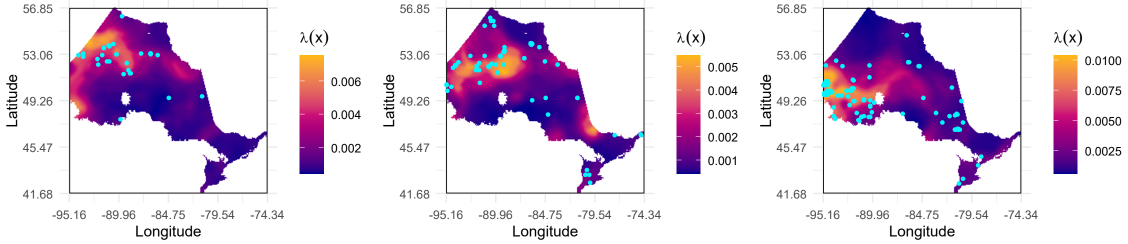

Figure 8: Left to right: Plug-in posterior means of the spatial intensity based on average temperature, precipitation level and wind speed, for the years $2013, 2015$ and 2021.

Here, we employed the same pre-processing of the covariates and the same values for the parameters of the prior as in the univariate analysis. The discretization of the (transformed) covariate space $[0,1]^3$ was obtained via a tetrahedral tessellation with $V = 970$ nodes (and maximum element volume equal to 0.001). The MCMC algorithm was iterated 20000 times (with 5000 burn-in samples), with pCN step-size equal to $\zeta = 0.1$.

5 Summary and discussion

In this article, we have considered the problem of estimating the intensity function of a covariate-driven point process from i.i.d. observations. We have devised novel multi-bandwidth Gaussian process methods, and shown that these achieve optimal adaptive posterior contraction rates towards (possibly) anisotropic ground truths (cf. Theorem 2.3). For implementation, we have constructed a Metropolis-within-Gibbs MCMC algorithm (cf. Section 2.4), relying on numerical likelihood evaluations and a dimension-robust sampling scheme. Our methods have been empirically assessed through numerical simulations (cf. Section 3), and applied to the analysis of a Canadian wildfire dataset (cf. Section 4). Overall, our investigation highlights the usefulness of the proposed strategy, which offers optimal reconstruction guarantees, a feasible implementation, and good practical performances.

5.1 Theoretical open problems

An important unexplored aspect of the problem are the statistical properties of the associated uncertainty quantification, since it is generally known that, in nonparametric statistical models, credible sets may have asymptotically vanishing frequentist coverage even if the posterior distribution is consistent, e.g. Diaconis & Freedman (1986). Potential directions to tackle this issue are the radius inflation strategy developed by Szabo et al. (2015), or the derivation of suitable 'nonparametric Bernstein-von Mises' theorems; see e.g. Castillo & Nickl (2013), and also Ray (2017) in the context of adaptive procedures. For both of these, the posterior contraction rates derived here could furnish a key 'localization' starting step.

Further, it would be of interest to extend our results to other nonparametric Bayesian procedures. It was recently shown by Giordano et al. (2025), in a different increasing domain regime, that covariate-based Pólya tree-type priors can achieve adaptive optimal point-wise posterior contraction rates. Since the local performance of Gaussian process methods is notoriously delicate to analyze, the latter could offer a flexible alternative also in the present scenario with i.i.d. observations. Related to this, let us also mention the important issue of developing rigorous statistical guarantees for alternative non-Bayesian strategies, including for kernel-type strategies constructed as in Guan (2008), Baddeley et al. (2012), Borrajo et al. (2020), for which our theoretical and empirical results may serve as a useful benchmark.

5.2 Extensions of the data analysis

While our approach appears to satisfactorily capture the relationship between the occurrence of wildfires and the considered covariates, several refinements are possible. Firstly, we acknowledge that yearly data on wildfires and meteorological conditions is likely to have intrinsic temporal correlations. These could be incorporated within the underlying probabilistic framework via auto-regressive components for both the point patterns and the covariates, or also by spatio-temporal models such as the one recently investigated by Miscouridou & Sulem (2026) (where, however, no covariates are considered). Additional covariates available in the Canadian Wildland Fire Information System website, as well as residual spatial effects along the lines of Remark 2.5, could be incorporated to improve predictive power, albeit at the risk of possibly over-parametrizing the model. Lastly, additional latent random effects could be included, assuming that

$$\lambda(x) = \rho(Z(x), Y(x)), \qquad x \in \mathcal{W},$$

where $Y := \{Y(x),\ x \in \mathcal{W}\}$ is an unobserved random field, modeled e.g. via a Gaussian process as in the Log-Gaussian Cox process of Møller et al. (1998). This could provide important robustness against latent spatial variability and dependencies, but it would require substantial modifications to present methodological and theoretical developments, that we leave for future research.

Data Availability Statement

The full data and R code are available at the URL: https://github.com/PatricDolmeta/Covariate-based-nonparametric-Bayesian-intensity-estimation.

References

Adams, R. P., Murray, I. & MacKay, D. J. C. (2009), Tractable nonparametric Bayesian inference in Poisson processes with Gaussian process intensities, *in* 'Proceedings of the 26th Annual International Conference on Machine Learning', ICML '09, Association for Computing Machinery, New York, NY, USA, pp. 9–16.

Agapiou, S., Dashti, M. & Helin, T. (2021), 'Rates of contraction of posterior distributions based on p-exponential priors', *Bernoulli* **27**(3), 1616–1642.

Baddeley, A., Chang, Y.-M., Song, Y. & Turner, R. (2012), 'Nonparametric estimation of the dependence of a spatial point process on spatial covariates', *Stat. Interface* **5**, 221–236.

Baddeley, A., Rubak, E. & Turner, R. (2016), *Spatial point patterns: methodology and applications with R*, Vol. 1, Chapman and Hall, CRC.

Bandyopadhyay, S. & Subba Rao, S. (2017), 'A test for stationarity for irregularly spaced spatial data', *J. R. Stat. Soc. Ser. B. Stat. Methodol.* **79**(1), 95–123.

Barron, A., Birgé, L. & Massart, P. (1999), 'Risk bounds for model selection via penalization', *Probab. Theory Relat. Fields.* **113**(3), 301–413.

Belitser, E., Serra, P. & van Zanten, H. (2015), 'Rate-optimal Bayesian intensity smoothing for inhomogeneous Poisson processes', *J. Statist. Plann. Inference* **166**, 24–35.

Bhattacharya, A., Pati, D. & Dunson, D. (2014), 'Anisotropic function estimation using multi-bandwidth Gaussian processes', *Ann. Stat.* **42**(1), 352.

Birgé, L. (2004), 'Model selection for Gaussian regression with random design', *Bernoulli* **10**(6), 1039 – 1051.

Borrajo, M. I., González-Manteiga, W. & Martínez-Miranda, M. D. (2020), 'Bootstrapping kernel intensity estimation for inhomogeneous point processes with spatial covariates', *Comput. Statist. Data Anal.* **144**, 106875, 21.

Brillinger, D. R. (1978), Comparative aspects of the study of ordinary time series and of point processes, *in* 'Developments in statistics, Vol. 1', Academic Press, New York-London, pp. 33–133.

Castillo, I. & Nickl, R. (2013), 'Nonparametric Bernstein–von Mises theorems in Gaussian white noise', *Ann. Statist.* **41**(4), 1999–2028.

Cotter, S. L., Roberts, G. O., Stuart, A. M. & White, D. (2013), 'MCMC methods for functions: Modifying old algorithms to make them faster', *Stat. Sci.* **28**(3).

Cox, D. R. (1955), 'Some statistical methods connected with series of events', *J. Roy. Statist. Soc. Ser. B* **17**, 129–157; discussion, 157–164.

Cressie, N. A. C. (2015), *Statistics for Spatial Data*, Wiley Classics Library, John Wiley & Sons, Inc., New York.

Diaconis, P. & Freedman, D. (1986), 'On the consistency of Bayes estimates', *Ann. Statist.* **14**(1), 1–26.

Diggle, P. J. (1990), 'A point process modelling approach to raised incidence of a rare phenomenon in the vicinity of a prespecified point', *J. R. Stat. Soc. Ser. A* **153**(3), 349–362.

Diggle, P. J. (2014), *Statistical Analysis of Spatial and Spatio-Temporal Point Patterns*, Vol. 128, third edn, CRC Press.

Diggle, P. J., Lange, N. & Beneš, F. M. (1991), 'Analysis of variance for replicated spatial point patterns in clinical neuroanatomy', *J. Am. Stat. Assoc.* **86**(415), 618–625.

DiMatteo, I., Genovese, C. R. & Kass, R. E. (2001), 'Bayesian curve-fitting with free-knot splines', *Biometrika* **88**(4), 1055–1071.

Dolmeta, P. & Giordano, M. (2025), Gaussian process methods for covariate-based intensity estimation, *in* 'International Workshop on Functional and Operatorial Statistics', Springer, pp. 185–192.

Donnet, S., Rivoirard, V., Rousseau, J. & Scricciolo, C. (2017), 'Posterior concentration rates for counting processes with Aalen multiplicative intensities', *Bayesian Anal.* **12**(1), 53–87.

Ghosal, S., Ghosh, J. K. & van der Vaart, A. W. (2000), 'Convergence rates of posterior distributions', *Ann. Statist.* **28**(2), 500–531.

Ghosal, S. & Van der Vaart, A. W. (2017), *Fundamentals of nonparametric Bayesian inference*, Cambridge University Press, Cambridge.

Giné, E. & Nickl, R. (2016), *Mathematical foundations of infinite-dimensional statistical models*, Cambridge University Press, New York.

Giordano, M. (2023), 'Besov-laplace priors in density estimation: optimal posterior contraction rates and adaptation', *Electron. J. Stat.* **17**(2), 2210–2249.

Giordano, M., Kirichenko, A. & Rousseau, J. (2025), 'Nonparametric Bayesian intensity estimation for covariate-driven inhomogeneous point processes', *Bernoulli (to appear)* .

Guan, Y. (2008), 'On consistent nonparametric intensity estimation for inhomogeneous spatial point processes', *J. Amer. Statist. Assoc.* **103**(483), 1238–1247.

Gugushvili, S. & Spreij, P. (2013), 'A note on non-parametric Bayesian estimation for Poisson point processes', *arXiv preprint arXiv:1304.7353* .

Gugushvili, S., Van Der Meulen, F., Schauer, M. & Spreij, P. (2018), 'Fast and scalable non-parametric bayesian inference for poisson point processes', *arXiv preprint arXiv:1804.03616* .

Haario, H., Saksman, E. & Tamminen, J. (2001), 'An adaptive Metropolis algorithm', *Bernoulli* **7**, 223–242.

Hairer, M., Stuart, A. M. & Vollmer, S. J. (2014), 'Spectral gaps for a Metropolis–Hastings algorithm in infinite dimensions', *Ann. Appl. Probab.* **24**(6), 2455–2490.

Hoffman, M. & Lepski, O. (2002), 'Random rates in anisotropic regression (with a discussion and a rejoinder by the authors)', *The Ann. Stat.* **30**(2), 325–396.

Illian, J. B., Sørbye, S. H. & Rue, H. v. (2012), 'A toolbox for fitting complex spatial point process models using integrated nested Laplace approximation (INLA)', *Ann. Appl. Stat.* **6**(4), 1499–1530.

Illian, J., Penttinen, A., Stoyan, H. & Stoyan, D. (2008), *Statistical analysis and modelling of spatial point patterns*, Statistics in Practice, John Wiley & Sons, Ltd., Chichester.

Juan, P., Mateu, J. & Saez, M. (2012), 'Pinpointing spatio-temporal interactions in wildfire patterns', *Stoch. Environ. Res. Risk Assess.* **26**, 1131–1150.

Kirichenko, A. & van Zanten, H. (2015), 'Optimality of Poisson processes intensity learning with Gaussian processes', *J. Mach. Learn. Res.* **16**, 2909–2919.

Koh, J., Pimont, F., Dupuy, J.-L. & Opitz, T. (2023), 'Spatiotemporal wildfire modeling through point processes with moderate and extreme marks', *Ann. Appl. Stat.* **17**(1), 560 – 582.

Kottas, A. & Sansó, B. (2007), 'Bayesian mixture modeling for spatial Poisson process intensities, with applications to extreme value analysis', *J. Statist. Plann. Inference* **137**(10), 3151–3163.

Kuo, L. & Ghosh, S. K. (1997), Bayesian nonparametric inference for nonhomogeneous poisson processes, Technical report, University of Connecticut, Department of Statistics.

Kutoyants, Y. A. (1998), *Statistical inference for spatial Poisson processes*, Vol. 134 of *Lecture Notes in Statistics*, Springer-Verlag, New York.

Lo, A. Y. (1982), 'Bayesian nonparametric statistical inference for Poisson point processes', *Z. Wahrsch. Verw. Gebiete* **59**(1), 55–66.

Miscouridou, X. & Sulem, D. (2026), 'Posterior concentration in spatio-temporal hawkes processes', *arXiv preprint arXiv:2601.03719* .

Møller, J., Syversveen, A. R. & Waagepetersen, R. P. (1998), 'Log Gaussian Cox processes', *Scand. J. Statist.* **25**(3), 451–482.

Nickl, R. (2023), *Bayesian Non-linear Statistical Inverse Problems*, Zurich Lectures in Advanced Mathematics, EMS Press.

Nyssbaum, M. (1987), 'Nonparametric estimation of a regression function that is smooth in a domain in $\mathbb{R}^k$', *Theory Probab. Its Appl.* **31**(1), 108–115.

Rasmussen, C. E. & Williams, C. K. I. (2005), *Gaussian Processes for Machine Learning*, The MIT Press.

Ray, K. (2017), 'Adaptive Bernstein–von Mises theorems in Gaussian white noise', *The Ann. Stat.* **45**(6), 2511–2536.

Rue, H., Martino, S. & Chopin, N. (2009), 'Approximate Bayesian inference for latent Gaussian models by using integrated nested Laplace approximations', *J. R. Stat. Soc. Ser. B* **71**(2), 319–392.

Silverman, B. W. (1986), *Density estimation for statistics and data analysis*, Monographs on Statistics and Applied Probability, Chapman & Hall, London.

Szabo, B., van der Vaart, A. & van Zanten, J. H. (2015), 'Frequentist coverage of adaptive nonparametric bayesian credible sets', *Ann. Statist.* **43**, 1391–1428.

van der Vaart, A. W. & van Zanten, J. H. (2008), 'Rates of contraction of posterior distributions based on Gaussian process priors', *Ann. Statist.* **36**(3), 1435–1463.

van der Vaart, A. W. & van Zanten, J. H. (2009), 'Adaptive Bayesian estimation using a Gaussian random field with inverse Gamma bandwidth', *Ann. Statist.* **37**(5B), 2655–2675.

Waagepetersen, R. P. (2007), 'An estimating function approach to inference for inhomogeneous Neyman-Scott processes', *Biometrics* **63**(1), 252–258, 315.

Yue, Y. R. & Loh, J. M. (2011), 'Bayesian semiparametric intensity estimation for inhomogeneous spatial point processes', *Biometrics* **67**(3), 937–946.

Supplementary Material

In this supplement, we present the proofs of all our results, additional simulations and further details on the data analysis.

A Proof of Theorem 2.3

As mentioned in Section 2.2, the main result holds under a slightly more flexible prior class, summarized in the following condition. The prior constructed in Section 2.1, which appears in the statement of Theorem 2.3, represents a concrete instance to which the general theory applies.

Condition A.1 (Multi-bandwidth Gaussian process priors for covariate-based intensities)**.** *Let $\mathcal{Z} \subset \mathbb{R}^d$, $d \in \mathbb{N}$, be a compact and convex set, and let $\mathcal{R}$ be the set of measurable, bounded and nonnegative-valued functions defined on $\mathcal{Z}$. Let Π be a prior supported on $\mathcal{R}$ given by the law of the random function $\rho(z) = \rho^*\sigma(w(z))$, $z \in \mathcal{Z}$, where:*

1. *$\sigma : \mathbb{R} \to (0, 1)$ is a smooth and strictly increasing function whose square-root is uniformly Lipschitz;*
2. *$\rho^* \sim \Pi_{\rho^*}$, for any absolutely continuous prior Π_{ρ^*} on $[0, c_{\rho^*} + \log n)$, for some fixed $c_{\rho^*} > 0$, whose p.d.f. (also denoted by Π_{ρ^*}) satisfies $\Pi_{\rho^*}(r) > 0$ for all $r \in [0, c_{\rho^*} + \log n)$.*
3. *Independently of ρ^*, $\ell = (\ell_1, \dots, \ell_d)$ with $\ell_1, \dots, \ell_d \overset{\text{iid}}{\sim} \Pi_\ell$, defined as follows: Let $\theta_1, \dots, \theta_d \overset{\text{iid}}{\sim} \Pi_\theta$ for any absolutely continuous distribution Π_θ on $[0, 1]$ whose p.d.f. (also denoted by Π_θ) satisfies $\Pi_\theta(t) > 0$ for all $t \in (0, 1)$. For each $j = 1, \dots, d$, given θ_j, set $\ell_j = \gamma_j^{\theta_j/d}$, where $\gamma_1, \dots, \gamma_d \overset{\text{iid}}{\sim} \Pi_\gamma$, for any absolutely continuous distribution Π_γ on $[0, \infty)$ whose p.d.f. (also denoted by Π_γ) satisfies*
$$c_\gamma g^{a_\gamma} e^{-b_\gamma g \log^{k_\gamma} g} \le \Pi_\gamma(g) \le C_\gamma g^{a_\gamma} e^{-B_\gamma g \log^{k_\gamma} g} \tag{17}$$
for all sufficiently large $g > 0$ and for universal constants $c_\gamma, C_\gamma, b_\gamma, B_\gamma > 0$ and $a_\gamma, k_\gamma \ge 0$.
4. *Independently of ρ^*, $w \sim \Pi_W$, defined as follows: Conditionally on $\ell_1, \dots, \ell_d \overset{\text{iid}}{\sim} \Pi_\ell$, let $w|\ell \sim \Pi_{W_\ell}$, given by the law of the restriction $W_\ell = \{W_\ell(z),\ z \in \mathcal{Z}\}$ to $\mathcal{Z}$ of a centered and stationary Gaussian process on $\mathbb{R}^d$ with kernel having spectral expansion*
$$\mathrm{E}[W_\ell(z)W_\ell(z')] = \int_{\mathbb{R}^d} e^{-i\sum_{j=1}^d \xi_j \ell_j (z_j - z'_j)} d\mu(\xi), \quad z = (z_1, \dots, z_d),\ z' = (z'_1, \dots, z'_d), \tag{18}$$
and whose spectral measure μ satisfies
$$\int_{\mathbb{R}^d} e^{c_\mu |\xi|} d\mu(\xi) < \infty \tag{19}$$
for some $c_\mu > 0$.

We refer to e.g. (Ghosal & Van der Vaart 2017, Chapter 11) for background information on stationary Gaussian processes. Below, for sets Θ, semi-metrics δ on Θ and any $\varepsilon > 0$, the covering numbers $\mathcal{N}(\varepsilon; \Theta, \delta)$ are defined as the smallest number of balls of δ-radius equal to ε required to cover Θ.

(of Theorem 2.3). We verify the conditions of the general concentration result below, Theorem B.1, with $\varepsilon_n = n^{-\alpha_0/(2\alpha_0+1)}\log^{c_1} n$ and $\bar\varepsilon_n = n^{-\alpha_0/(2\alpha_0+1)}\log^{(2c_1+2+d)/2} n$ for some sufficiently large $c_1 > 0$. Write shorthand $\|\cdot\|_\infty = \|\cdot\|_{L^\infty(\mathcal{Z})}$. Since ρ_0 is continuous and $\mathcal{Z}$ is compact, we have $\|\rho\|_\infty < c_{\rho^*} + \log n$ provided that n is large enough, whence, for all such n's, $\|\rho_0\|_\infty$ is included in the interior of the support of Π_{ρ^*}. Following the argument in Section 4.1 of Kirichenko & van Zanten (2015), we may write $\rho_0 = (\|\rho_0\|_\infty + 1)\sigma\circ w_0$, where $w_0 : \mathcal{Z} \to \mathbb{R}$ is given by $w_0 := \sigma^{-1}\circ(\rho_0/(\|\rho_0\|_\infty + 1))$. Since ρ_0 is bounded away from zero by assumption, the function $\rho_0/(\|\rho_0\|_\infty + 1)$ too is bounded away from zero. Noting that also $\rho_0/(\|\rho_0\|_\infty + 1) < 1$, we may then conclude that $w_0 \in C^\alpha(\mathcal{Z})$ in view of the fact that σ^{-1} is smooth over (0,1).

We start with the verification of the prior mass condition (24). We have

$$\begin{aligned}
&\Pi(\rho : \|\rho - \rho_0\|_\infty \le \varepsilon_n)\\
&\quad = \Pi\left((\rho^*, w) : \|(\rho^* - (\|\rho_0\|_\infty + 1))\sigma\circ w + (\|\rho_0\|_\infty + 1)(\sigma\circ w - \sigma\circ w_0)\|_\infty \le \varepsilon_n\right)\\
&\quad \ge \Pi_{\rho^*}\left(r : |r - (\|\rho_0\|_\infty + 1)| \le \varepsilon_n/2\right)\Pi_W\left(w : \|\sigma\circ w - \sigma\circ w_0\|_\infty \le \varepsilon_n/(2\|\rho_0\|_\infty + 2)\right).
\end{aligned}$$

Since Π_{ρ^*} has a positive and continuous density by assumption and since $n\varepsilon_n^2 \to \infty$, the first probability is bounded below by $c_3\varepsilon_n \ge e^{-n\varepsilon_n^2}$ as $n \to \infty$ for some $c_3 > 0$. Further, note that since $\sqrt{\sigma}$ is Lipschitz by assumption and since $\sigma \le 1$, the function σ too is Lipschitz (with Lipschitz constant bounded by twice that of $\sqrt{\sigma}$), whence the second probability is greater than $\Pi_W(w : \|w - w_0\|_\infty \le c_4\varepsilon_n)$ for some $c_4 > 0$. For ε_n as above, provided that c_1 is large enough, the latter is bounded below by $e^{-n\varepsilon_n^2}$ by Lemma A.2. This shows that condition (24) holds (with $C_1 = 2$).

Moving onto the sieve condition (25), for $\mathcal{B}_n$ the set defined as in Lemma A.3 below, take

$$\mathcal{R}_n := \bigcup_{r\le c_{\rho^*}+\log n} r\mathcal{S}_n, \qquad \mathcal{S}_n := \{\sigma\circ w,\ w\in\mathcal{B}_n\}.$$

Then, recalling the prior construction from Condition A.1,

$$\Pi(\mathcal{R}_n^c) = \int_0^{c_{\rho^*}+\log n} \Pi_W\left(w : r\sigma\circ w \notin \mathcal{R}_n\right)\Pi_{\rho^*}(r)dr.$$

For all $r \le c_{\rho^*} + \log n$, we have $\Pi_W(w : r\sigma\circ w \notin \mathcal{R}_n) \le \Pi_W(w : \sigma\circ w \notin \mathcal{S}_n) \le \Pi_W(\mathcal{B}_n^c)$. By Lemma A.3, for any $C_2 > 1$, we may choose the sequences η_n, R_n, T_n in the definition of $\mathcal{B}_n$ so that $\eta_n \le \bar\varepsilon_n/\sqrt{c_{\rho^*} + \log n}$ and $\Pi_W(\mathcal{B}_n^c) \le e^{-C_2 n\varepsilon_n^2}$. Combined with the previous display, this shows that $\Pi(\mathcal{R}_n^c) \le e^{-C_2 n\varepsilon_n^2}$. Further, for $\bar\varepsilon_n$ as above, the set $\mathcal{B}_n$ also satisfies

$$\log\mathcal{N}(\bar\varepsilon_n/\sqrt{c_{\rho^*} + \log n}; \mathcal{B}_n, \|\cdot\|_\infty) \le \log\mathcal{N}(\eta_n; \mathcal{B}_n, \|\cdot\|_\infty) \lesssim n\bar\varepsilon_n^2 \tag{20}$$

by Lemma A.3. We proceed verifying the sup-norm metric entropy inequality (26), which, as observed in Remark B.2, is a sufficient condition for the complexity bound in (25) to hold. Since $\sqrt{\sigma}$ is bounded and Lipschitz by assumption we have, for any $r_1, r_2 \in [0, c_{\rho^*} + \log n)$ and any $w_1, w_2 \in \mathcal{B}_n$,

$$\begin{aligned}
\|\sqrt{r_1\sigma\circ w_1} - \sqrt{r_2\sigma\circ w_2}\|_\infty &\le |\sqrt{r_1} - \sqrt{r_2}| + c_6\sqrt{c_{\rho^*} + \log n}\|w_1 - w_2\|_\infty\\
&\le \sqrt{|r_1 - r_2|} + c_6\sqrt{c_{\rho^*} + \log n}\|w_1 - w_2\|_\infty
\end{aligned}$$

for some $c_6 > 0$ only depending on σ. Therefore, in view of (20),

$$\begin{aligned}
&\log\mathcal{N}\left(\bar{\varepsilon}_n; \sqrt{\mathcal{R}_n}, \|\cdot\|_\infty\right) \\
&\quad \leq \log\mathcal{N}\left(\bar{\varepsilon}_n/2; [0, c_{\rho^*} + \log n], \sqrt{|\cdot|}\right) + \log\mathcal{N}(\bar{\varepsilon}_n/(2c_6\sqrt{c_{\rho^*} + \log n}); \mathcal{B}_n, \|\cdot\|_\infty) \\
&\quad \lesssim \log((c_{\rho^*} + \log n)/\bar{\varepsilon}_n) + n\bar{\varepsilon}_n^2 \lesssim n\bar{\varepsilon}_n^2.
\end{aligned}$$

The claim of Theorem 2.3 now follows from an application of Theorem B.1 with the choice $M = c_{\rho^*} + \log n$, upon setting $C = c_1 + 2 + d/2$. □

A.1 Prior mass for multi-bandwidth Gaussian processes with independent length-scales

The following lemma provides a lower bound, required in the proof of Theorem 2.3, for the probability of small sup-norm neighborhoods charged by the randomly re-scaled Gaussian prior Π_W defined in Condition A.1. The result extends the third claim of Theorem 3.1 in Bhattacharya et al. (2014) to the present construction with independent length-scales.

Lemma A.2. *For $\alpha = (\alpha_1, \dots, \alpha_d) \in (0, \infty)^d$, let $w_0 \in C^\alpha(\mathcal{Z})$, and let Π_W be a prior for w constructed as in Condition A.1. Then, there exists a constant $K_1 > 0$ only depending on w_0, d and the spectral measure μ from (19) such that, for all sufficiently small $\varepsilon > 0$,*

$$\Pi_W\left(w : \|w - w_0\|_{L^\infty(\mathcal{Z})} \leq \varepsilon\right) \geq e^{-(1/\varepsilon)^{1/\alpha_0}\log^{K_1}(1/\varepsilon)}, \qquad \alpha_0 = 1/\sum_{j=1}^d \alpha_j^{-1}.$$

In particular, setting $\varepsilon_n = n^{-\alpha_0/(2\alpha_0+1)}\log^{K_2} n$ for any $K_2 > K_1\alpha_0/(2\alpha_0 + 1)$, it holds for all sufficiently large n that

$$\Pi_W\left(w : \|w - w_0\|_{L^\infty(\mathcal{Z})} \leq \varepsilon_n\right) \geq e^{-n\varepsilon_n^2}. \tag{21}$$

Proof. Write shorthand $\|\cdot\|_\infty = \|\cdot\|_{L^\infty(\mathcal{Z})}$. Let $\varepsilon > 0$, and let $\ell = (\ell_1, \dots, \ell_d)$, $\ell_1, \dots, \ell_d \overset{\text{iid}}{\sim} \Pi_\ell$ and $w|\ell \sim \Pi_{W_\ell}$ be as in Condition A.1. Then, we have

$$\begin{aligned}
&\Pi_W\left(w : \|w - w_0\|_\infty \leq \varepsilon\right) \\
&\quad = \int_0^\infty \cdots \int_0^\infty \Pi_W\left(w : \|w - w_0\|_\infty \leq \varepsilon | \ell_1, \dots, \ell_d\right) d\Pi_\ell(\ell_1) \dots d\Pi_\ell(\ell_d) \\
&\quad = \int_0^\infty \cdots \int_0^\infty \Pi_{W_\ell}\left(w : \|w - w_0\|_\infty \leq \varepsilon\right) d\Pi_\ell(\ell_1) \dots d\Pi_\ell(\ell_d).
\end{aligned}$$

Let $\ell^* = \prod_{j=1}^d \ell_j$, $\bar{\ell} = \max_{j=1,\dots,d} \ell_j$ and $\underline{\ell} = \min_{j=1,\dots,d} \ell_j$. By a combination of Lemmas 4.2 and 4.3 of Bhattacharya et al. (2014), for any fixed $\ell_0 > 0$ there exist constants $\varepsilon_0 \in (0, 1/2)$ and $c_1, c_2 > 0$ only depending on w_0, d and μ such that

$$\Pi_{W_\ell}\left(w : \|w - w_0\|_\infty \leq \varepsilon\right) \geq e^{-c_1\ell^*\log^{1+d}(\bar{\ell}/\varepsilon)},$$

for all $\varepsilon < \varepsilon_0$ and all ℓ such that $\underline{\ell} > \ell_0$ and $\sum_{j=1}^d \ell_j^{-\alpha_j} \leq d\varepsilon/c_2$. Thus, provided that

$\varepsilon < \varepsilon_0 \wedge c_2 \ell_0^{-\overline{\alpha}}$,

$$\begin{aligned}
&\Pi_W\left(w : \|w - w_0\|_\infty \le \varepsilon\right)\\
&\quad\ge \int_{(c_2/\varepsilon)^{1/\alpha_1}}^{2(c_2/\varepsilon)^{1/\alpha_1}} \cdots \int_{(c_2/\varepsilon)^{1/\alpha_d}}^{2(c_2/\varepsilon)^{1/\alpha_d}} e^{-c_1 \ell^* \log^{1+d}(\bar{\ell}/\varepsilon)} d\Pi_\ell(\ell_1) \dots d\Pi_\ell(\ell_d)\\
&\quad\ge e^{-c_1 2^d c_2^{1/\alpha_0} (1/\varepsilon)^{1/\alpha_0} \log^{1+d}(2 c_2^{1/\underline{\alpha}} \varepsilon^{-1-1/\underline{\alpha}})} \int_{(c_2/\varepsilon)^{1/\alpha_1}}^{2(c_2/\varepsilon)^{1/\alpha_1}} \cdots \int_{(c_2/\varepsilon)^{1/\alpha_d}}^{2(c_2/\varepsilon)^{1/\alpha_d}} d\Pi_\ell(\ell_1) \dots d\Pi_\ell(\ell_d)\\
&\quad\ge e^{-(1/\varepsilon)^{1/\alpha_0} \log^{c_3}(1/\varepsilon)} \prod_{j=1}^{d} \int_{(c_2/\varepsilon)^{1/\alpha_j}}^{2(c_2/\varepsilon)^{1/\alpha_j}} d\Pi_\ell(\ell_j)
\end{aligned}$$

for any constant $c_3 > 1 + d$. Set $\Theta_j := \{t \in [0,1] : c_4/\log(1/\varepsilon) < t - d\alpha_0/\alpha_j < 2c_4/\log(1/\varepsilon)\}$, $j = 1, \dots, d$, for some fixed $c_4 > 0$. Then, recalling the construction of Π_ℓ from Condition A.1, for all ε small enough,

$$\begin{aligned}
\int_{(c_2/\varepsilon)^{1/\alpha_j}}^{2(c_2/\varepsilon)^{1/\alpha_j}} d\Pi_\ell(\ell_j) &\ge \int_{\Theta_j} \left(\int_{(c_2/\varepsilon)^{1/\alpha_j}}^{2(c_2/\varepsilon)^{1/\alpha_j}} \Pi_\gamma(g^{d/t}) \frac{d}{t} g^{d/t-1} dg \right) \Pi_\theta(t) dt\\
&\gtrsim \int_{\Theta_j} \frac{1}{t} \left(\int_{(c_2/\varepsilon)^{1/\alpha_j}}^{2(c_2/\varepsilon)^{1/\alpha_j}} g^{(1+a_\gamma)d/t-1} e^{-b_\gamma (d/t)^{k_\gamma} g^{d/t} \log^{k_\gamma} g} dg \right) \Pi_\theta(t) dt\\
&\gtrsim \int_{\Theta_j} \frac{1}{t} e^{-(d/t)^{k_\gamma} (1/\varepsilon)^{d/(t\alpha_j)} \log^{c_5}(1/\varepsilon)} \Pi_\theta(t) dt,
\end{aligned}$$

for some $c_5 > 0$. For each $t \in \Theta_j$, provided that ε is small enough, we have that $c_6 < t \le 1$ for some sufficiently small $c_6 > 0$ that does not depend on j. Further,

$$\frac{(1/\varepsilon)^{d/(t\alpha_j)}}{(1/\varepsilon)^{1/\alpha_0}} = \left(\frac{1}{\varepsilon}\right)^{-(t\alpha_j - d\alpha_0)/(d\alpha_0^2 + \alpha_0(t\alpha_j - d\alpha_0))} \le e^{-\frac{c_4 \alpha_j}{\log(1/\varepsilon)(d\alpha_0^2 + 2\alpha_0 c_4/\log(1/\varepsilon))} \log(1/\varepsilon)} \le c_7$$

for $c_7 > 0$ independent of j. It follows that the second to last display is lower bounded by

$$e^{-(1/\varepsilon)^{1/\alpha_0} \log^{c_8}(1/\varepsilon)} \int_{\Theta_j} \Pi_\theta(t) dt \ge e^{-(1/\varepsilon)^{1/\alpha_0} \log^{c_9}(1/\varepsilon)}$$

for some $c_8, c_9 > 0$ independent of j, having used the fact that Θ_j contains an interval of width proportional to $1/\log(1/\varepsilon)$, whence its prior probability under Π_θ is at least a (universal) constant times $1/\log(1/\varepsilon)$. Combining the obtained estimates yields the first claim of Lemma A.2. The second then readily follows for the given choice of ε_n. □

A.2 Sieves for multi-bandwidth Gaussian processes with independent length-scales

We construct sieves with bounded complexity containing the bulk of the mass of the randomly re-scaled Gaussian prior Π_W defined in Condition A.1, employed in the proof of Theorem 2.3. Our construction is similar to the one on p. 373 of Bhattacharya et al. (2014), which is itself based on ideas from van der Vaart & van Zanten (2009). In fact, in the proof, we exploit the observation that our prior with independent length-scales allows to construct sieves with overall smaller metric entropy compared to the ones obtained with the Dirichlet-based hyper-prior used in (Bhattacharya et al. 2014, Section 3.1). In view of the small ball estimate (21) and Lemma A.3 below, we expect that priors based on Π_W achieve adaptive anisotropic posterior contraction rates in other statistical models as well, along the lines discussed for example in (van der Vaart & van Zanten 2008, Section 3).

Let $\mathcal{C}_1$ denote the unit ball in sup-norm of $C(\mathcal{Z})$. For each $\ell \in (0,\infty)^d$, let $\mathcal{H}_\ell$ be the reproducing kernel Hilbert space associated to the Gaussian process W_ℓ from Condition A.1, and let $\mathcal{H}_{\ell,1}$ denote its unit ball; see (Bhattacharya et al. 2014, Section 4.1) for definitions and properties. For $\eta, R, T > 0$, construct the sets

$$\mathcal{B} := \eta\mathcal{C}_1 + \bigcup_{\vartheta\in[0,1]^d} \bigcup_{\ell \le R^{\vartheta/d}} T\mathcal{H}_{\ell,1}, \tag{22}$$

having denoted $R^{\vartheta/d} := (R^{\theta_1/d}, \dots, R^{\theta_d/d})$ for any $\vartheta = (\theta_1, \dots, \theta_d) \in [0,1]^d$.

Lemma A.3. *Let Π_W be a prior for w constructed as in Condition A.1. Then, for all sufficiently small η, all R large enough, and all $T \ge 2\sqrt{2}\sqrt{R}\log^{(1+d)/2}(R/\eta)$,*

$$\Pi_W(\mathcal{B}^c) \le \frac{1}{2}e^{-R\log^{1+d}(R/\eta)} + R^{a_\gamma}e^{-B_\gamma R}, \qquad \log\mathcal{N}(\eta;\mathcal{B},\|\cdot\|_{L^\infty(\mathcal{Z})}) \lesssim R\log^{1+d}(2T/\eta),$$

where $a_\gamma, B_\gamma > 0$ are the constants from (17). In particular, if $\varepsilon_n = n^{-\alpha_0/(2\alpha_0+1)}\log^{K_1} n$ for some $\alpha_0, K_1 > 0$, then for any $K_2 > 0$, letting $\mathcal{B}_n$ be as in (22) with $\eta = \eta_n = n^{-K_3}\log^{K_4} n$ for any $K_3 \ge \alpha_0/(2\alpha_0+1)$ and any $K_4 > 0$, $R = R_n = K_5 n^{1/(2\alpha_0+1)}\log^{2K_1} n$ for any $K_5 > K_2/(B_\gamma \wedge 1)$, and $T = T_n = 2\sqrt{2}K_5 n^{1/(4\alpha_0+2)}\log^{(2K_1+1+d)/2} n$, we have that

$$\Pi_W(\mathcal{B}^c) \le e^{-K_2 n\varepsilon_n^2}, \qquad \log\mathcal{N}(\eta_n;\mathcal{B}_n,\|\cdot\|_{L^\infty(\mathcal{Z})}) \lesssim n\bar{\varepsilon}_n^2,$$

for all n large enough, where $\bar{\varepsilon}_n = n^{-\alpha_0/(2\alpha+1)}\log^{(2K_1+1+d)/2} n$.

Proof. We start with the verification of the first inequality in the first claim. For $\vartheta = (\theta_1, \dots, \theta_d) \in [0,1]^d$, and for $\eta, R, T > 0$, set

$$\mathcal{B}^\vartheta := \eta\mathcal{C}_1 + \bigcup_{\ell \le R^{\vartheta/d}} T\mathcal{H}_{\ell,1}. \tag{23}$$

Then, with Π_{W_ℓ} and Π_ℓ as in Condition A.1, we have

$$\begin{aligned}\Pi_W((\mathcal{B}^\vartheta)^c|\theta_1,\dots,\theta_d) &= \int_0^\infty \cdots \int_0^\infty \Pi_{W_\ell}((\mathcal{B}^\vartheta)^c)d\Pi_\ell(\ell_1|\theta_1)\dots d\Pi_\ell(\ell_d|\theta_d)\\ &\le \int_0^{R^{\theta_1/d}} \cdots \int_0^{R^{\theta_d/d}} \Pi_{W_\ell}((\mathcal{B}^\vartheta)^c)d\Pi_\ell(\ell_1|\theta_1)\dots d\Pi_\ell(\ell_d|\theta_d)\\ &\quad + \sum_{j=1}^d \Pi_\ell(l > R^{\theta_j/d}|\theta_j).\end{aligned}$$

Since $\mathcal{B}^\vartheta$ contains the set $\eta\mathcal{C}_1 + T\mathcal{H}_{\ell,1}$ for any $\ell \le R^{\vartheta/d}$ by construction, by Borell's isoperimetric inequality (Giné & Nickl 2016, Theorem 2.6.12),

$$\begin{aligned}\Pi_{W_\ell}((\mathcal{B}^\vartheta)^c) &\le \Pi_{W_\ell}((\eta\mathcal{C}_1 + T\mathcal{H}_{\ell,1})^c)\\ &\le 1 - \Phi\left(T + \Phi^{-1}\left(\Pi_{W_\ell}(\eta\mathcal{C}_1)\right)\right) \le 1 - \Phi\left(T + \Phi^{-1}\left(\Pi_{W_{R^{\vartheta/d}}}(\eta\mathcal{C}_1)\right)\right),\end{aligned}$$

where Φ is the standard normal cumulative distribution function, whose inverse we denote by Φ^{-1}. The last inequality follows from the fact that Φ and Φ^{-1} are monotone increasing and that, for all $\ell \le R^{\vartheta/d}$,

$$\begin{aligned}\Pi_{W_{R^{\vartheta/d}}}(\eta\mathcal{C}_1) &= \Pi_{W_1}\left(w : \sup_{z\in\mathcal{Z}}\left| w\left(\sum_{j=1}^d R^{\theta_j/d} z_j\right)\right| \le \eta\right)\\ &\le \Pi_{W_1}\left(w : \sup_{z\in\mathcal{Z}}\left| w\left(\sum_{j=1}^d \ell_j z_j\right)\right| \le \eta\right) = \Pi_{W_\ell}(\eta\mathcal{C}_1),\end{aligned}$$

in view of the stationarity of W_1 and the convexity of $\mathcal{Z}$. Provided that ε is small enough and R is sufficiently large, Lemma 4.3 in Bhattacharya et al. (2014) gives that

$$\Pi_{W_{R^{\vartheta/d}}}(\eta\mathcal{C}_1) \ge e^{-R^{\sum_{j=1}^d \theta_j/d}\log^{1+d}(R^{\bar{\vartheta}/d}/\eta)} \ge e^{-R\log^{1+d}(R/\eta)},$$

having used the fact that $0 \le \theta_j \le 1$ for all j. By the standard inequality $\Phi^{-1}(t) \ge -\sqrt{2\log(1/t)}$ holding for all $0 < t < 1$, cf. (van der Vaart & van Zanten 2009, Lemma 4.10), we then obtain

$$\Pi_{W_\ell}((\mathcal{B}^\vartheta)^c) \le 1 - \Phi\left(T - \sqrt{2R}\log^{(1+d)/2}(R/\eta)\right),$$

whence, taking $T \ge 2\sqrt{2}\sqrt{R}\log^{(1+d)/2}(R/\eta)$, the standard Gaussian tail bound yields

$$\Pi_{W_\ell}((\mathcal{B}^\vartheta)^c) \le 1 - \Phi\left(\sqrt{2}\sqrt{R}\log^{(1+d)/2}(R/\eta)\right) \le \frac{1}{2}e^{-R\log^{1+d}(R/\eta)}.$$

Finally, since, by construction, $\ell_j^{d/\theta_j}|\theta_j \overset{\text{iid}}{\sim} \Pi_\gamma$ for each $j = 1,\dots,d$, with Π_γ satisfying (17), we have for all R large enough

$$\Pi_\ell(l > R^{\theta_j/d}|\theta_j) = \Pi_\ell(l^{d/\theta_j} > R|\theta_j) \le \frac{2C_\gamma R^{a_\gamma}}{B_\gamma \log^{k_\gamma} R}e^{-B_\gamma R\log^{k_\gamma} R} \le R^{a_\gamma}e^{-B_\gamma R},$$

cf. (van der Vaart & van Zanten 2009, Lemma 4.9). Combining the obtained estimates implies that for all $\vartheta \in [0,1]^d$, all sufficiently small η, all R large enough, and all $T \ge (C_1 - \sqrt{2})\sqrt{R}\log^{(1+d)/2}(R/\eta)$,

$$\Pi_W((\mathcal{B}^\vartheta)^c|\theta_1,\dots,\theta_d) \le \frac{1}{2}e^{-R\log^{1+d}(R/\eta)} + R^{a_\gamma}e^{-B_\gamma R}.$$

We then see that the set $\mathcal{B}$ defined in (25) with η, R and T as above verifies the first inequality in the first claim of Lemma A.3 since, using the fact that $\mathcal{B}^\vartheta \subseteq \mathcal{B}$ for all $\vartheta \in [0,1]^d$ by construction,

$$\begin{aligned}\Pi_W(\mathcal{B}^c) &= \int_0^1\cdots\int_0^1 \Pi_W(\mathcal{B}^c|\theta_1,\dots,\theta_d)d\Pi_\theta(\theta_1)\dots d\Pi_\theta(\theta_d)\\ &\le \int_0^1\cdots\int_0^1 \Pi_W((\mathcal{B}^\vartheta)^c|\theta_1,\dots,\theta_d)d\Pi_\theta(\theta_1)\dots d\Pi_\theta(\theta_d)\\ &\le \frac{1}{2}e^{-R\log^{1+d}(R/\eta)} + R^{a_\gamma}e^{-B_\gamma R}.\end{aligned}$$

Moving onto the second claim, write $\|\cdot\|_\infty = \|\cdot\|_{L^\infty(\mathcal{Z})}$, and note that, by construction, $\mathcal{B}$ is a η-enlargement in sup-norm of the set $\bigcup_{\vartheta\in[0,1]^d}\bigcup_{\ell\le R^{\vartheta/d}} T\mathcal{H}_{\ell,1}$, and

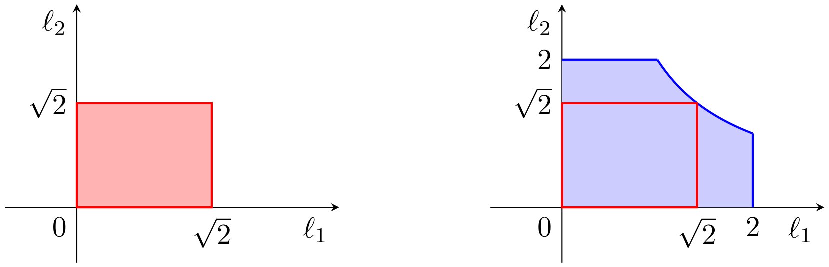

Figure 9: Left, shaded red: the set of length-scales $\bigcup_{(\theta_1,\theta_2)\in[0,1]^2}\{(\ell_1,\ell_2) : 0 \le \ell_1 \le R^{\theta_1/2}, 0 \le \ell_2 \le R^{\theta_2/2}\}$, for $R = 2$. Right, shaded blue: the set of length-scales $\bigcup_{(\theta_1,\theta_2)\in\Delta_2}\{(\ell_1,\ell_2) : 0 \le \ell_1 \le R^{\theta_1}, 0 \le \ell_2 \le R^{\theta_2}\}$.

.

therefore,

$$\log \mathcal{N}(\eta; \mathcal{B}, \|\cdot\|_{L^\infty(\mathcal{Z})}) \le \log \mathcal{N}\left(\eta/2; \bigcup_{\vartheta\in[0,1]^d} \bigcup_{\ell \le R^{\vartheta/d}} T\mathcal{H}_{\ell,1}, \|\cdot\|_\infty\right).$$

Let Δ_{d-1} be the $d-1$ dimensional simplex. Then, provided that $R > 1$,

$$\bigcup_{\vartheta\in[0,1]^d} \bigcup_{\ell\le R^{\vartheta/d}} T\mathcal{H}_{\ell,1} \subseteq \bigcup_{\vartheta\in\Delta_{d-1}} \bigcup_{\ell\le R^{\vartheta}} T\mathcal{H}_{\ell,1}$$

due to the fact that

$$\bigcup_{\vartheta\in[0,1]^d} \left\{(\ell_1,\dots,\ell_d) : 0 \le \ell_j \le R^{\theta_j/d},\ j = 1,\dots,d\right\}$$
$$= [0, R^{1/d}]^d \subseteq \bigcup_{\vartheta\in\Delta_{d-1}} \left\{(\ell_1,\dots,\ell_d) : 0 \le \ell_j \le R^{\theta_j},\ j = 1,\dots,d\right\},$$

cf. Figure 9. Thus, using Lemma 4.5 in Bhattacharya et al. (2014),

$$\log \mathcal{N}(\eta; \mathcal{B}, \|\cdot\|_\infty) \le \log \mathcal{N}\left(\eta/2; \bigcup_{\vartheta\in\Delta_{d-1}} \bigcup_{\ell\le R^{\vartheta}} T\mathcal{H}_{\ell,1}, \|\cdot\|_\infty\right) \le c_3 R \log^{1+d}(2T/\eta),$$

for some $c_3 > 0$ only depending on d and the spectral measure μ in (19). This concludes the verification of the first claim of Lemma A.3.

For the second claim, with the given definition of $\mathcal{B}_n$, we have

$$\Pi(\mathcal{B}_n^c) \le \frac{1}{2} e^{-K_2 n^{1/(2\alpha_0+1)} \log^{2K_1} n} + \frac{1}{2} e^{-K_2 n^{1/(2\alpha_0+1)} \log^{2K_1} n} = e^{-K_2 n \varepsilon_n^2},$$

as well as

$$\log \mathcal{N}(\eta_n; \mathcal{B}_n, \|\cdot\|_\infty) \lesssim n^{1/(2\alpha_0+1)} \log^{2K_1} n \log^{1+d} n = n\bar{\varepsilon}_n^2.$$

□

B A general posterior contraction rate theorem

In this section, we present a general concentration theorem holding under abstract prior conditions resembling the standard assumptions from the asymptotic theory of

Bayesian nonparametrics (e.g. Ghosal & Van der Vaart (2017)). This constitutes the primary tool to prove our main result on multi-bandwidth Gaussian process methods for covariate-based intensities, Theorem 2.3. The general result is based on the Hellinger testing approach to posterior contraction rates in i.i.d. statistical models of Ghosal et al. (2000), which we pursue in the present setting by extending ideas developed by Belitser et al. (2015) and Kirichenko & van Zanten (2015) for non-covariate-dependent inhomogeneous Poisson processes. Recall the metric d_Z defined in (7), and the notation $\mathcal{R}$ for the set of measurable, bounded and nonnegative-valued functions defined on the covariate space $\mathcal{Z}$.

Theorem B.1. *Let $\rho_0 \in \mathcal{R}$ satisfy $\inf_{z\in\mathcal{Z}} \rho_0(z) > 0$, and consider data $D^{(n)} \sim P^{(n)}_{\rho_0}$ arising as described at the beginning of Section 2. Let Π be a prior for ρ supported on $\mathcal{R}$, and assume that for a sequence $\varepsilon_n \to 0$ such that $n\varepsilon_n^2 \to \infty$ as $n \to \infty$ and some constant $C_1 > 0$ we have*

$$\Pi(\rho : \|\rho - \rho_0\|_{L^\infty(\mathcal{Z})} \le \varepsilon_n) \ge e^{-C_1 n\varepsilon_n^2}. \tag{24}$$

Further, assume that for a sequence $\bar{\varepsilon}_n \to 0$ as $n \to \infty$ such that $\bar{\varepsilon}_n \ge \varepsilon_n$, and for all $C_2 > 1$, there exist measurable sets $\mathcal{R}_n \subseteq \mathcal{R}$ and some constant $C_3 > 0$ such that,

$$\Pi(\mathcal{R}_n^c) \le e^{-C_2 n\varepsilon_n^2}; \qquad \log \mathcal{N}(\bar{\varepsilon}_n; \mathcal{R}_n, d_Z) \le C_3 n\bar{\varepsilon}_n^2. \tag{25}$$

Then, for all $M > 1$ and all sufficiently large $L > 0$,

$$\Pi\left(\rho : d_Z(\rho \wedge M, \rho_0 \wedge M) > LM\bar{\varepsilon}_n \middle| D^{(n)}\right) \to 0$$

in $P^{(\infty)}_{\rho_0}$-probability as $n \to \infty$.

The proof of Theorem B.1 is in Section B.1 below. The 'prior mass condition' (24) entails the customary requirement that Π put sufficient probability mass on neighborhoods of ρ_0 with small radius in sup-norm. In the present setting, the latter can be shown to control the Kullback-Leibler divergence and variation (cf. Lemma B.3).

The 'sieve condition' (25) requires that the bulk of the prior mass be concentrated on sets of suitably bounded metric entropy. The complexity bound in the second inequality is with respect to the metric d_Z from (7), which is natural in view of its close relationship to the Hellinger distance (cf. Lemma B.4). As argued in Remark B.2 below, d_Z is upper bounded by the sup-norm of the difference between square-rooted intensities. This furnishes a standard approach to verify assumption (25) for a potentially large variety of nonparametric priors via analytic results on their information geometry, including the novel ones for multi-bandwidth Gaussian processes with independent length-scales derived in Section A.2. On the other hand, for certain priors, sup-norm complexity bounds are known to be possibly too restrictive. This is the case, for example, for Besov-Laplace priors, which are popular in inverse problems and imaging, where they furnish a 'spatially inhomogeneous' alternative to Gaussian priors; see Agapiou et al. (2021), as well as the discussion after Theorem 1 in Giordano (2023). Extensions of the results presented in this article to such priors may still be pursued in the stationary setting considered in Section 2.3, under which d_Z is equivalent to an L^2-distance between square-rooted intensities, giving rise to weaker complexity bounds compared to the sup-norm.

The claim of Theorem B.1 involves the cut-off of ρ and ρ_0 at any arbitrary level M. This stems from the lower bound for the Hellinger distance from Lemma B.4, and is likely an artifact of the proof arising from the presence of random covariates; see Section 7.3.2 of Ghosal & Van der Vaart (2017) for a similar situation in nonparametric regression. We note that the cut-off imposes little restriction, since M can be taken arbitrarily large, only (linearly) impacting the constant pre-multiplying the rate. In particular, for $M > \|\rho_0\|_{L^\infty(\mathcal{Z})}$, we may replace $\rho_0 \wedge M$ with ρ_0 in the claim of Theorem B.1. Further, the cut-off may be sidestepped altogether if Π is supported on a subset of functions with values on an interval of the form $[0, \rho_n^*]$ for some slowly increasing $\rho_n^* \to \infty$, in which case the obtained rate is $\rho_n^* \varepsilon_n$. This approach was taken for the construction of the prior in Condition A.1 with the choice $\rho_n^* = c_{\rho^*} + \log n$, only slightly impacting the logarithmic factor appearing in the claim of in Theorem 2.3.

Remark B.2 (Sup-norm complexity bounds)**.** *Since $\mathcal{W}$ is compact, we have that*

$$d_Z^2(\rho_1, \rho_2) \leq \mathrm{E}\left[\int_{\mathcal{W}} \sup_{x \in \mathcal{W}} \left|\sqrt{\rho_1(Z(x))} - \sqrt{\rho_2(Z(x))}\right|^2 dx\right] = \mathrm{vol}(\mathcal{W}) \|\sqrt{\rho_1} - \sqrt{\rho_2}\|^2_{L^\infty(\mathcal{Z})}.$$

A sufficient condition for (25) to hold is then that

$$\log \mathcal{N}\left(\varepsilon_n; \sqrt{\mathcal{R}_n}, \|\cdot\|_{L^\infty(\mathcal{Z})}\right) \leq C_3 n \varepsilon_n^2, \tag{26}$$

for some $C_3 > 0$, where $\sqrt{\mathcal{R}_n} := \{\sqrt{\rho},\ \rho \in \mathcal{R}_n\}$. This is similar to the metric entropy condition employed by Belitser et al. (2015) in the context of non-covariate-dependent inhomogeneous Point processes, except with the sup-norm replacing the L^2-distance.

B.1 Proof of Theorem B.1

We verify the conditions for concentration in Hellinger distance in i.i.d. statistical models from Theorem 8.9 in Ghosal & Van der Vaart (2017). Define the neighborhoods

$$B_n := \left\{\rho : KL(p_{\rho_0}, p_\rho) \leq c_1 \varepsilon_n^2,\ V(p_{\rho_0}, p_\rho) \leq c_1 \varepsilon_n^2\right\}, \qquad c_1 > 0,$$

where KL and V denote the Kullback-Leibler divergence and variation, respectively, defined as in (27) below. Since $\varepsilon_n \to 0$ as $n \to \infty$, Lemma B.3 implies that for all sufficiently large n, provided that c_1 is large enough, $\{\rho : \|\rho - \rho_0\|_{L^\infty(\mathcal{Z})} \leq \varepsilon_n\} \subseteq B_n$. In view of assumption (24), we then have $\Pi(B_n) \geq e^{-C_1 n \varepsilon_n^2}$, yielding condition (8.4) of Theorem 8.9 in Ghosal & Van der Vaart (2017).

Next, fix $C_2 > C_1 + 4$, let $\mathcal{R}_n$ be the corresponding set from assumption (25), and define the collection of observational densities $\mathcal{P}_n := \{p_\rho,\ \rho \in \mathcal{R}_n\}$, with p_ρ as in (2). Then $\Pi(\rho : p_\rho \notin \mathcal{P}_n) \leq \Pi(\mathcal{R}_n^c) \leq e^{-(C_1+4)n\varepsilon_n^2}$. Further, for h the Hellinger distance defined in (31), the upper bound from Lemma B.4 implies that

$$\log \mathcal{N}(\sqrt{2}\bar{\varepsilon}_n; \mathcal{P}_n, h) \leq \log \mathcal{N}(\bar{\varepsilon}_n; \mathcal{R}_n, d_Z) \lesssim n \bar{\varepsilon}_n^2.$$

This shows that conditions (8.5) and (8.6) of Theorem 8.9 in Ghosal & Van der Vaart (2017) are also verified. Conclude that $\Pi(\cdot|D^{(n)})$ contracts towards ρ_0 in Hellinger distance at rate ε_n, namely that for all sufficiently large $c_2 > 0$,

$$\Pi\left(\rho : h(p_\rho, p_{\rho_0}) > c_2 \bar{\varepsilon}_n \middle| D^{(n)}\right) \to 0$$

in $P_{\rho_0}^{(\infty)}$-probability as $n \to \infty$. For all $M > 1$, the claim of Theorem B.1 then follows in view of the lower bound from Lemma B.4, upon taking $L > 0$ a sufficiently large multiple of c_2. □

B.2 Bounds for the Kullback-Leibler divergence and variation

For pairs (N, Z) arising as described at the beginning of Section 2, recall the expression of the observational densities p_ρ, $\rho \in \mathcal{R}$, given by (2), with dominating measure P_1 corresponding to the standard Poisson case. The associated Kullback-Leibler divergence and variation are defined, respectively, as

$$KL(p_{\rho_0}, p_\rho) := E_{\rho_0}\left[\log \frac{p_{\rho_0}(N,Z)}{p_\rho(N,Z)}\right]; \qquad V(p_{\rho_0}, p_\rho) := Var_{\rho_0}\left[\log \frac{p_{\rho_0}(N,Z)}{p_\rho(N,Z)}\right]. \tag{27}$$

The following lemma provides upper bounds for these two quantities in terms of the sup-norm distance $\|\rho - \rho_0\|_{L^\infty(\mathcal{Z})}$. It is based on ideas from the proof of Lemma 1 and Theorem 1 of Belitser et al. (2015), with suitable adaptations to accommodate the presence of random covariates.

Lemma B.3. *Let $\rho_0 \in \mathcal{R}$ satisfy $\inf_{z\in\mathcal{Z}} \rho_0(z) > 0$. Then, there exist constants $C_1, C_2 > 0$ only depending on ρ_0 such that, for all sufficiently small $\varepsilon \in (0,1)$ and all $\rho \in \mathcal{R}$ satisfying $\|\rho - \rho_0\|_{L^\infty(\mathcal{Z})} \le \varepsilon$, we have*

$$KL(p_{\rho_0}, p_\rho) \le C_1\varepsilon^2; \qquad V(p_{\rho_0}, p_\rho) \le C_2\varepsilon^2.$$

Proof. By the tower property of conditional expectations,

$$KL(p_{\rho_0}, p_\rho) = \mathrm{E}\left[E_{\rho_0}\left[\log \frac{p_{\rho_0}(N,Z)}{p_\rho(N,Z)}\middle| Z\right]\right], \tag{28}$$

where the outer expectation is intended with respect to the law of Z. We have

$$\frac{p_{\rho_0}(N,Z)}{p_\rho(N,Z)} = e^{\sum_{k=1}^K \log \frac{\rho_0(Z(X_k))}{\rho(Z(X_k))} - \int_{\mathcal{W}}(\rho_0(Z(x)) - \rho(Z((x)))dx},$$

and using the fact that, under P_{ρ_0}, $N|Z$ is distributed as an inhomogeneous Poisson process with intensity $\lambda_{\rho_0} = \rho_0 \circ Z$, the inner expectation in (28) equals

$$\begin{aligned}
&-\int_{\mathcal{W}} (\rho_0(Z(x)) - \rho(Z(x)))dx + E_{\rho_0}\left[\sum_{k=1}^K \log \frac{\rho_0(Z(X_k))}{\rho(Z(X_k))}\middle| Z\right] \\
&\quad = -\int_{\mathcal{W}} (\rho_0(Z(x)) - \rho(Z(x)))dx + \int_{\mathcal{W}} \log \frac{\rho_0(Z(x))}{\rho(Z(x))}\rho_0(Z(x))dx \\
&\quad = \int_{\mathcal{W}} \rho_0(Z(x))\left(\frac{\rho(Z(x))}{\rho_0(Z(x))} - 1 - \log\frac{\rho(Z(x))}{\rho_0(Z(x))}\right)dx = \int_{\mathcal{W}} \rho_0(Z(x))G\left(\frac{\rho(Z(x))}{\rho_0(Z(x))}\right)dx,
\end{aligned}$$

having set $G(t) := t - 1 - \log t$, $t > 0$, and having used the standard formula for the expectation of functionals of inhomogeneous Poisson processes. The function G satisfies $|G(t)| \le 3(\sqrt{t} - 1)^2$ for all $t \in (1/e, \infty)$ and $|G(t)| \le |\log t|$ for all $t \in (0, 1/e]$. It follows that

$$\begin{aligned}
E_{\rho_0}\left[\log \frac{p_{\rho_0}(N,Z)}{p_\rho(N,Z)}\middle| Z\right] &\le 3\int_{\{x:\rho(Z(x))/\rho_0(Z(x))>1/e\}} \left(\sqrt{\rho(Z(x))} - \sqrt{\rho_0(Z(x))}\right)^2 dx \\
&\quad + \int_{\{x:\rho(Z(x))/\rho_0(Z(x))\le 1/e\}} \rho_0(Z(x))\left|\log\frac{\rho(Z(x))}{\rho_0(Z(x))}\right| dx \\
&\le 3\left\|\sqrt{\lambda_{\rho_0}} - \sqrt{\lambda_\rho}\right\|^2_{L^2(\mathcal{W})} + \int_{\mathcal{W}} \rho_0(Z(x))\log^2\frac{\rho(Z(x))}{\rho_0(Z(x))}dx.
\end{aligned}$$

Using the fact that $1-t \leq |\log t|$ for all $t \in (0,1)$, we obtain the further upper bound

$$\begin{aligned}\left\|\sqrt{\lambda_{\rho_0}} - \sqrt{\lambda_\rho}\right\|^2_{L^2(\mathcal{W})} &\leq \int_{\{x:\rho(Z(x))\geq\rho_0(Z(x))\}} \rho(Z(x)) \left(\log\sqrt{\frac{\rho_0(Z(x))}{\rho(Z(x))}}\right)^2 dx \\ &\quad + \int_{\{x:\rho_0(Z(x))>\rho(Z(x))\}} \rho_0(Z(x)) \left(\log\sqrt{\frac{\rho(Z(x))}{\rho_0(Z(x))}}\right)^2 dx \\ &\leq \frac{1}{4}\int_{\mathcal{W}} (\rho_0(Z(x)) \vee \rho(Z(x))) \log^2 \frac{\rho_0(Z(x))}{\rho(Z(x))} dx.\end{aligned}$$

Combined with the second to last display, this implies

$$E_{\rho_0}\left[\log\frac{p_{\rho_0}(N,Z)}{p_\rho(N,Z)}\middle| Z\right] \leq \frac{7}{4}\int_{\mathcal{W}} (\rho(Z(x)) \vee \rho_0(Z(x))) \log^2 \frac{\rho_0(Z(x))}{\rho(Z(x))} dx. \tag{29}$$

Now for each $x \in \mathcal{W}$, by a Taylor expansion with exact remainder,

$$\log\frac{\rho_0(Z(x))}{\rho(Z(x))} = \left(\frac{\rho_0(Z(x))}{\rho(Z(x))} - 1\right) - \frac{1}{2\xi_x^2}\left(\frac{\rho_0(Z(x))}{\rho(Z(x))} - 1\right)^2,$$

where ξ_x lies between $\rho_0(Z(x))/\rho(Z(x))$ and 1. Since ρ_0 is bounded away from zero by assumption, for all sufficiently small $\varepsilon \in (0,1)$, we have that if $\|\rho-\rho_0\|_{L^\infty(\mathcal{Z})} \leq \varepsilon$ then necessarily $\inf_{z\in\mathcal{Z}}\rho(z) \geq \frac{1}{2}\inf_{z\in\mathcal{Z}}\rho_0(z) > 0$. It follows that

$$\left|\frac{\rho_0(Z(x))}{\rho(Z(x))} - 1\right| \leq \frac{1}{\inf_{z\in\mathcal{Z}}\rho(z)}\|\rho_0-\rho\|_\infty \leq c_1\varepsilon,$$

for some $c_1 > 0$ independent of ρ, x and ε. This also implies that ξ_x is itself bounded away from zero, so that

$$\frac{1}{2\xi_x^2}\left(\frac{\rho_0(Z(x))}{\rho(Z(x))} - 1\right)^2 \leq c_2\varepsilon^2 \leq c_2\varepsilon,$$

and $\log^2(\rho_0(Z(x))/\rho(Z(x))) \leq c_3\varepsilon^2$, with $c_2, c_3 > 0$ independent of ρ, x and ε. Finally, observing that, if ε is sufficiently small, we must have $\|\rho\|_{L^\infty(\mathcal{Z})} \leq 2\|\rho_0\|_{L^\infty(\mathcal{Z})}$, we obtain from (29) that

$$E_{\rho_0}\left[\log\frac{p_{\rho_0}(N,Z)}{p_\rho(N,Z)}\middle| Z\right] \leq \frac{7}{2}\|\rho_0\|_{L^\infty(\mathcal{Z})} c_3 \mathrm{vol}(\mathcal{W})\varepsilon^2. \tag{30}$$

Combined with (28), this concludes the proof of the first claim of Lemma B.3 upon taking $C_1 := \frac{7}{2}c_3\|\rho_0\|_{L^\infty(\mathcal{Z})}\mathrm{vol}(\mathcal{W})$.

The second claim is proved with a similar argument, applying the law of total variance to obtain the identity

$$V(p_{\rho_1}, p_{\rho_2}) = \mathrm{E}\left[Var_{\rho_0}\left[\log\frac{p_{\rho_0}(N,Z)}{p_\rho(N,Z)}\middle| Z\right]\right] + \mathrm{Var}\left[E_{\rho_0}\left[\log\frac{p_{\rho_0}(N,Z)}{p_\rho(N,Z)}\middle| Z\right]\right],$$

where the outer expectation and variance are intended with respect to the law of Z. Using again the fact that, under P_{ρ_0}, $N|Z$ is distributed as a inhomogeneous Poisson process with intensity λ_{ρ_0},

$$
\begin{aligned}
Var_{\rho_0}\left[\log\frac{p_{\rho_0}(N,Z)}{p_\rho(N,Z)}\middle| Z\right] &= Var_{\rho_0}\left[\sum_{i=1}^K \log\frac{\rho_0(Z(X_i))}{\rho(Z(X_i))} - \int_{\mathcal{W}}(\rho_0(Z(x)) - \rho(Z(x))dx\middle| Z\right]\\
&= Var_{\rho_0}\left[\sum_{i=1}^K \log\frac{\rho_0(Z(X_i))}{\rho(Z(X_i))}\middle| Z\right] = \int_{\mathcal{W}} \log^2\frac{\rho_0(Z(x))}{\rho(Z(x))}\rho_0(Z(x))dx.
\end{aligned}
$$

The bounds obtained in the first part of the proof now yield that, for all sufficiently small $\varepsilon \in (0,1)$, if $\|\rho - \rho_0\|_{L^\infty(\mathcal{Z})} \le \varepsilon$ we must have

$$
Var_{\rho_0}\left[\log\frac{p_{\rho_0}(N,Z)}{p_\rho(N,Z)}\middle| Z\right] \le c_3\|\rho_0\|_{L^\infty(\mathcal{Z})}\mathrm{vol}(\mathcal{W})\varepsilon^2,
$$

where we recall that the constant c_3 is independent of ρ, x and ε. Further, in view of (30), we also have

$$
\mathrm{Var}\left[E_{\rho_0}\left[\log\frac{p_{\rho_0}(N,Z)}{p_\rho(N,Z)}\middle| Z\right]\right] \le c_4\varepsilon^4 \le c_4\varepsilon^2,
$$

for some $c_4 > 0$ independent of ρ, x and ε. Setting $C_2 := c_3\|\rho_0\|_{L^\infty(\mathcal{Z})}\mathrm{vol}(\mathcal{W}) + c_4$ yields the second claim of Lemma B.3. □

B.3 Bounds for the Hellinger distance

The Hellinger distance between two observational densities p_ρ, p_{ρ_0}, with $\rho, \rho_0 \in \mathcal{R}$, defined as in (2), is given by

$$
h\left(p_{\rho_1}, p_{\rho_2}\right) := \sqrt{E_1\left[\left(\sqrt{p_{\rho_1}(N,Z)} - \sqrt{p_{\rho_2}(N,Z)}\right)^2\right]}, \qquad \rho_1, \rho_2 \in \mathcal{R}, \tag{31}
$$

where E_1 is the expectation with respect to the dominating measure P_1. The following lemma provides upper and lower bounds for this quantity in terms of the metric d_Z from (7). Its proof adapts, in the present setting, the argument to derive the first statement of Lemma 1 in Belitser et al. (2015).

Lemma B.4. *For all $\rho_1, \rho_2 \in \mathcal{R}$ and all $M > 0$ it holds that*

$$
\frac{2(1 - e^{-\frac{1}{2}M\mathrm{vol}(\mathcal{W})})}{M\mathrm{vol}(\mathcal{W})} d_Z^2(\rho_1 \wedge M, \rho_2 \wedge M) \le h^2\left(p_{\rho_1}, p_{\rho_2}\right) \le 2d_Z^2(\rho_1, \rho_2).
$$

Proof. We start with the well-known identity for the square Hellinger distance,

$$
h^2\left(p_{\rho_1}, p_{\rho_2}\right) = 2\left[1 - a\left(p_{\rho_1}, p_{\rho_2}\right)\right], \tag{32}
$$

where $a\left(p_{\rho_1}, p_{\rho_2}\right) := E_1\left[\sqrt{p_{\rho_1}(N,Z)}\sqrt{p_{\rho_2}(N,Z)}\right]$ is the Hellinger affinity. By a change of measure and the tower property of conditional expectations, the latter can be written as

$$
\begin{aligned}
a\left(p_{\rho_1}, p_{\rho_2}\right) &= E_1\left[\sqrt{\frac{p_{\rho_1}(N,Z)}{p_{\rho_2}(N,Z)}}p_{\rho_2}(N,Z)\right]\\
&= E_{\rho_2}\left[\sqrt{\frac{p_{\rho_1}(N,Z)}{p_{\rho_2}(N,Z)}}\right] = \mathrm{E}\left[E_{\rho_2}\left[\sqrt{\frac{p_{\rho_1}(N,Z)}{p_{\rho_2}(N,Z)}}\middle| Z\right]\right],
\end{aligned}
$$

where the outer expectation is intended with respect to the law of Z. Recalling (2) and using the fact that, under P_{ρ_2}, $N|Z$ is distributed as an inhomogeneous Poisson point process with intensity λ_{ρ_2}, the inner expectation in the last display equals

$$\begin{aligned}
&e^{-\frac{1}{2}\int_{\mathcal{W}}(\lambda_{\rho_1}(x)-\lambda_{\rho_2}(x))dx} E_{\rho_2}\left[e^{\frac{1}{2}\sum_{k=1}^{K}\log\frac{\lambda_{\rho_1}(X_k)}{\lambda_{\rho_2}(X_k)}} \middle| Z \right] \\
&\quad = e^{-\frac{1}{2}\int_{\mathcal{W}}(\lambda_{\rho_1}(x)-\lambda_{\rho_2}(x))dx} e^{\int_{\mathcal{W}}\left(1-\sqrt{\lambda_{\rho_1}(x)/\lambda_{\rho_2}(x)}\right)\lambda_{\rho_2}(x)dx} = e^{-\frac{1}{2}\|\sqrt{\lambda_{\rho_1}}-\sqrt{\lambda_{\rho_2}}\|^2_{L^2(\mathcal{W})}}.
\end{aligned}$$

This implies that $a\left(p_{\rho_1}, p_{\rho_2}\right) = \mathrm{E}\left[e^{-\frac{1}{2}\|\sqrt{\lambda_{\rho_1}}-\sqrt{\lambda_{\rho_2}}\|^2_{L^2(\mathcal{W})}}\right]$, which combined with (32) yields

$$h^2\left(p_{\rho_1}, p_{\rho_2}\right) = 2\left(1 - \mathrm{E}\left[e^{-\frac{1}{2}\|\sqrt{\lambda_{\rho_1}}-\sqrt{\lambda_{\rho_2}}\|^2_{L^2(\mathcal{W})}}\right]\right). \tag{33}$$

The upper bound in the statement of Lemma B.4 then follows from Jensen's inequality and an application of the fact that $1 - e^{-t} \leq t$ for all $t \in \mathbb{R}$, whence

$$h^2\left(p_{\rho_1}, p_{\rho_2}\right) \leq 2\left(1 - e^{-\frac{1}{2}\mathrm{E}\|\sqrt{\lambda_{\rho_1}}-\sqrt{\lambda_{\rho_2}}\|^2_{L^2(\mathcal{W})}}\right) \leq 2\mathrm{E}\left\|\sqrt{\lambda_{\rho_1}} - \sqrt{\lambda_{\rho_2}}\right\|^2_{L^2(\mathcal{W})} = 2d_Z^2(\rho_1, \rho_2).$$

For the lower bound, we apply ideas from the proof of Proposition 1 in Birgé (2004). We observe that for all $M > 0$,

$$\begin{aligned}
\|\sqrt{\lambda_{\rho_1\wedge M}} - \sqrt{\lambda_{\rho_2\wedge M}}\|^2_{L^2(\mathcal{W})} &= \int_{\mathcal{W}}\left(\sqrt{\rho_1(Z(x))\wedge M} - \sqrt{\rho_2(Z(x))\wedge M}\right)^2 dx \\
&\leq \int_{\mathcal{W}}\left(\sqrt{\rho_1(Z(x))} - \sqrt{\rho_2(Z(x))}\right)^2 dx = \left\|\sqrt{\lambda_{\rho_1}} - \sqrt{\lambda_{\rho_2}}\right\|^2_{L^2(\mathcal{W})},
\end{aligned}$$

whence, in view of (33),

$$h^2\left(p_{\rho_1}, p_{\rho_2}\right) \geq 2\left(1 - \mathrm{E}\left[e^{-\frac{1}{2}\|\sqrt{\lambda_{\rho_1\wedge M}}-\sqrt{\lambda_{\rho_2\wedge M}}\|^2_{L^2(\mathcal{W})}}\right]\right).$$

At the same time, $\left\|\sqrt{\lambda_{\rho_1\wedge M}} - \sqrt{\lambda_{\rho_2\wedge M}}\right\|^2_{L^2(\mathcal{W})} \leq M\mathrm{vol}(\mathcal{W})$, and by using the inequality, holding for all $0 \leq t_1 \leq t_2$,

$$e^{-t_1} \leq \frac{e^{-t_2} - 1}{t_2} t_1 + 1,$$

cf. (Birgé 2004, p. 1043), with the choices $t_1 = \frac{1}{2}\left\|\sqrt{\lambda_{\rho_1\wedge M}} - \sqrt{\lambda_{\rho_2\wedge M}}\right\|^2_{L^2(\mathcal{W})}$ and $t_2 = \frac{1}{2}M\mathrm{vol}(\mathcal{W})$, we obtain

$$\begin{aligned}
h^2\left(p_{\rho_1}, p_{\rho_2}\right) &\geq \frac{2(1 - e^{-\frac{1}{2}M\mathrm{vol}(\mathcal{W})})}{M\mathrm{vol}(\mathcal{W})}\mathrm{E}\left\|\sqrt{\lambda_{\rho_1\wedge M}} - \sqrt{\lambda_{\rho_2\wedge M}}\right\|^2_{L^2(\mathcal{W})} \\
&= \frac{2(1 - e^{-\frac{1}{2}M\mathrm{vol}(\mathcal{W})})}{M\mathrm{vol}(\mathcal{W})} d_Z^2(\rho_1 \wedge M, \rho_2 \wedge M).
\end{aligned}$$

□

C Further simulation results

We expand the numerical simulation studies from Section 3, providing additional experiments with different ground truths, as well as various diagnostic plots for the MCMC algorithm described in Section 2.4, which we have employed throughout to approximately sample from the posterior distributions. We further empirically investigate the performance of our approach in the presence of purely spatial effects and over-parametrization.

C.1 Additional experiments with univariate covariates

On the observation window $\mathcal{W} = [-1/2, 1/2]^2$, we take the univariate covariate random field Z from Section 3.1, and consider the recovery of two additional ground truths, respectively defined as:

1. A simple exponentially-decaying intensity function, cf. Figure 10 (top row),

$$\rho_0(z) = 2e^{3(1-z)-1}, \qquad z \in [0,1]; \tag{34}$$

2. A more volatile intensity function with both positive and negative deviations from a flat baseline, cf. Figure 10 (bottom row),

$$\rho_0(z) = 2 + 2P\Big(z; \frac{3}{4}, a\Big) - 2P\Big(z; \frac{1}{4}, a\Big), \qquad a = \frac{3}{8}, \qquad z \in [0,1], \tag{35}$$

   where $P(z; c, a) = 1 - p(2\delta(z,c)/a)$ is the 'plateau function' centered at $c \in \mathbb{R}$ and with width $a/2 > 0$. Above, we have denoted by $\delta(z,c)$ the absolute distance of z from c up to period $1/2$, and by p the smooth polynomial $p(t) = 0.6t^5 - 15t^4 + 10t^3$ clamped to $[0,1]$.

For both of these, we simulated independent realizations of N and Z as outlined in Section 3.1, and, for each set of observations, performed posterior inference via the Metropolis-within-Gibbs sampling scheme from Section 2.4. All the prior (hyper-)hyperparameters, as well as all the tuning parameters for the implementation of the MCMC algorithm, were specified exactly as in the experiments described in Section 3.1. Figure 10 displays the obtained posterior means and point-wise 95%-credible intervals under increasing sample sizes $n = 250, 500, 1000$, as well as averaged kernel estimates (defined as in (13)). The (relative) L^2-estimation errors, averaged across 100 replications of each experiment, and their standard deviations, are reported in Table 3. The results are broadly in line with the ones from the experiments presented in Section 3.1, corroborating the conclusions drawn therein, and empirically supporting the theoretical findings from Section 2.2.

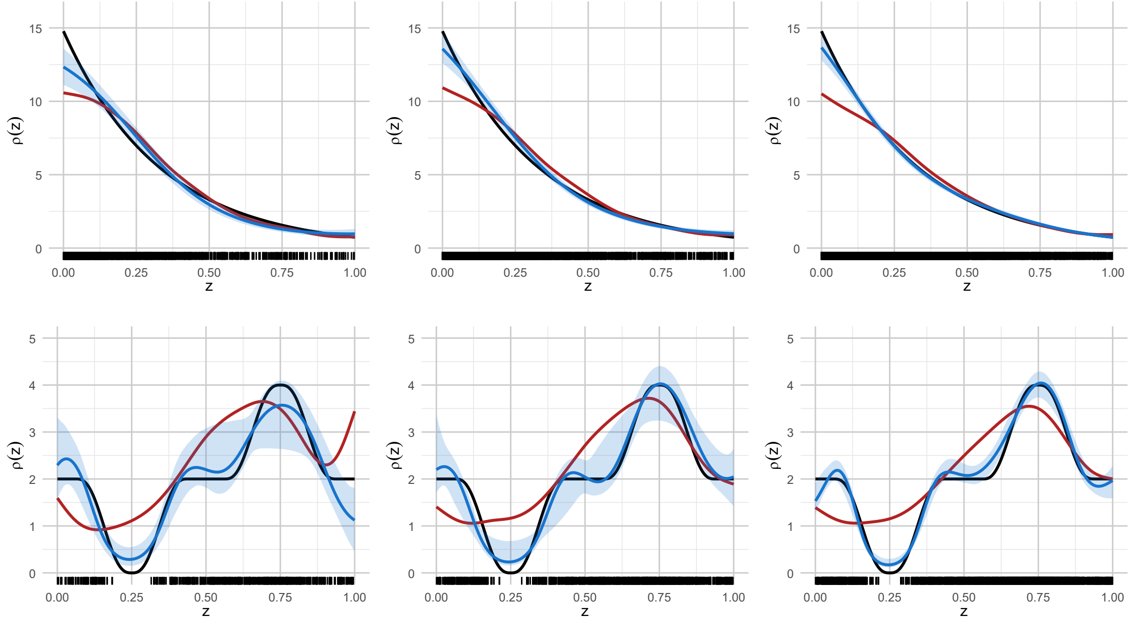

Figure 10: Top row, left to right: Posterior means (solid blue), pointwise 95%-credible intervals (shaded blue), averaged kernel estimates (solid red) for $n = 250, 500, 1000$. The ground truth (34) is shown in solid black. Bottom row: Estimates for the true intensity (35).

ρ_0		$n = 50$	$n = 250$	$n = 500$	$n = 1000$
(34)	$\Vert\hat{\rho}_{\Pi}^{(n)} - \rho_0\Vert_{L^2}/\Vert\rho_0\Vert_{L^2}$	0.22 (0.043)	0.13 (0.023)	0.07 (0.013)	0.04 (0.01)
	$\Vert\hat{\rho}_{\kappa} - \rho_0\Vert_{L^2}/\Vert\rho_0\Vert_{L^2}$	0.21 (0.04)	0.21 (0.03)	0.18 (0.02)	0.19 (0.008)
(35)	$\Vert\hat{\rho}_{\Pi}^{(n)} - \rho_0\Vert_{L^2}/\Vert\rho_0\Vert_{L^2}$	0.37 (0.04)	0.22 (0.03)	0.17 (0.04)	0.15 (0.03)
	$\Vert\hat{\rho}_{\kappa} - \rho_0\Vert_{L^2}/\Vert\rho_0\Vert_{L^2}$	0.33 (0.11)	0.36 (0.24)	0.34 (0.16)	0.27 (0.06)

Table 3: Average relative L^2-estimation errors (and their standard deviations) over 100 repeated experiments for the posterior mean $\hat{\rho}_{\Pi}^{(n)}$ and the averaged kernel estimate $\hat{\rho}_{\kappa}$. For ρ_0 as in (34), $\Vert\rho_0\Vert_{L^2} = 6.09$; for ρ_0 as in (35), $\Vert\rho_0\Vert_{L^2} = 2.29$.

C.2 Additional experiments with bivariate covariates

For the bi-dimensional scenario, we consider covariates $Z(x) = (Z_1(x), Z_2(x))$ constructed as in Section 3.2. Figure 11 shows three realizations of the bivariate covariate process, where the difference in the length-scales between Z_1 and Z_2 (0.005 and 0.05, respectively) can be visualized.

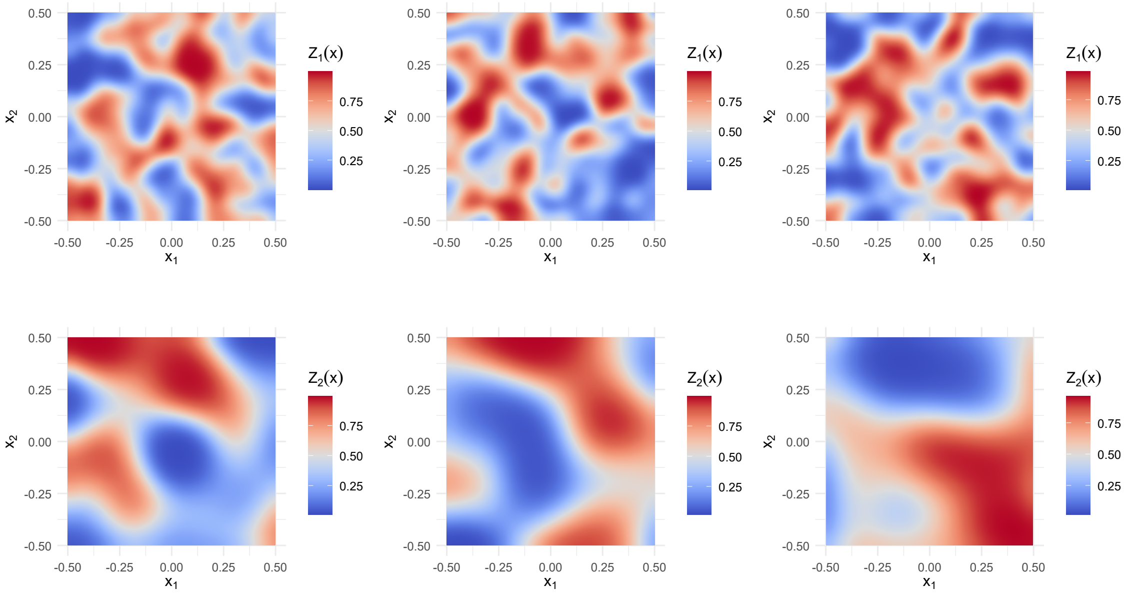

Figure 11: Independent realizations of the bivariate covariate process. The top row is relative to Z_1, while the bottom row is relative to Z_2.

Next, we construct two additional true covariate-based intensities, respectively defined as:

1.
$$\rho_0(z_1, z_2) = \max\left\{0,\ 30 - 90\ f_{SN}\left(z_1, z_2,\ (0.3, 0.3),\ 0.5I_2,\ (-1,-1)\right)\right\}, \tag{36}$$
for $(z_1, z_2) \in [0,1]^2$, where I_2 is the identity matrix in $\mathbb{R}^{2,2}$ and f_{SN} denotes the (bi-dimensional) skew-normal p.d.f., cf. Figure 12 (last panel);

2.
$$\begin{aligned}\rho_0&(z_1, z_2)\\ &= 6f_{SN}(z_1, z_2; (0.3, 0.8), 0.03I_2, (-1,-1)) + 14f_{SN}(z_1, z_2; (0.7, 0.2), 0.05I_2, (3,-2)),\end{aligned} \tag{37}$$
for $(z_1, z_2) \in [0,1]^2$, cf. Figure 14 (last panel).

The obtained estimates for the ground truth from (36) are shown in Figures 12 and 13. For an enhanced visualization, the latter displays the one-dimensional projections of the posterior means along the two diagonals of the covariate space $\mathcal{Z} = [0,1]^2$. This allows to more clearly asses the quality of the reconstruction of important features of the true intensity, such as the peak located in the top-right corner, and the depression concentrated in the bottom part. Results for the ground truth (37) are shown in Figure (36). Table 4 reports the estimation errors. The performance of the averaged kernel estimates is also included.

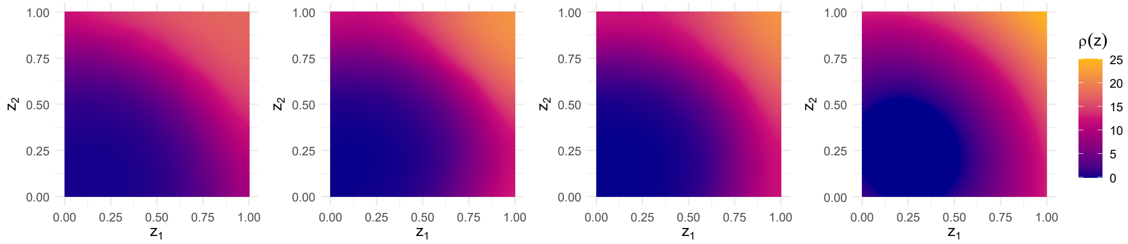

Figure 12: Left to right: Posterior means for $n = 50, 250, 1000$, and the ground truth (36).

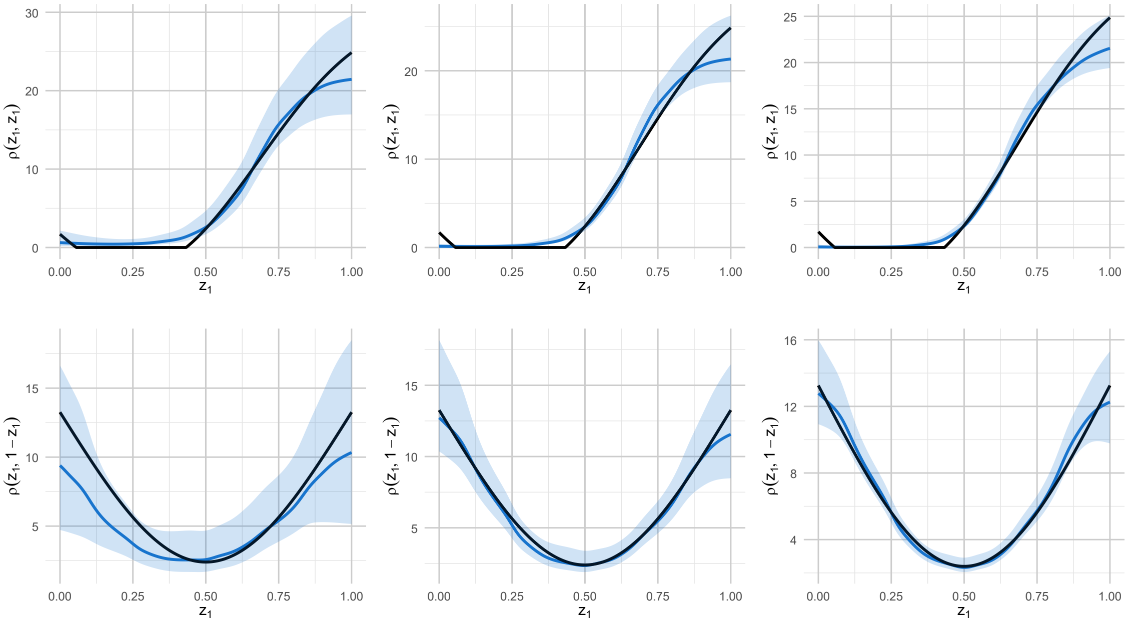

Figure 13: Top row, left to right: Projections of the posterior means (solid blue) along the principal diagonal, and associated pointwise 95%-credible intervals (shaded blue). The solid black line represents the projection of the ground truth, $\rho_0(z_1, z_1),\ z_1 \in [0, 1]$, for ρ_0 as in (36). Bottom row: projections on the anti-diagonal. The solid black line shows the projection $\rho_0(z_1, 1 - z_1),\ z_1 \in [0, 1]$.

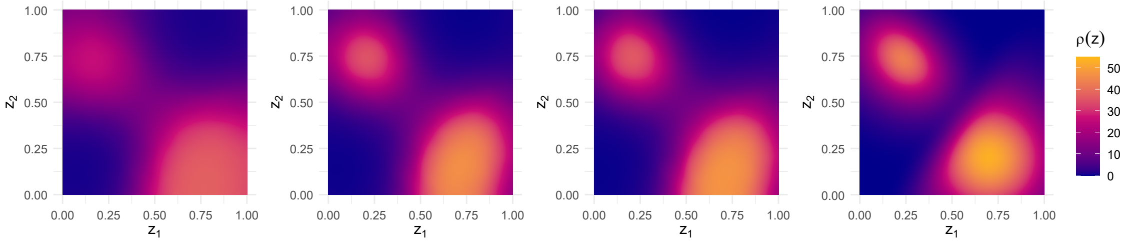

Figure 14: Left to right: Posterior means for $n = 50, 250, 1000$, and the ground truth (37).

ρ_0		$n = 10$	$n = 50$	$n = 250$	$n = 1000$
(36)	$\Vert\hat{\rho}_{\Pi}^{(n)} - \rho_0\Vert_{L^2}/\Vert\rho_0\Vert_{L^2}$	0.32 (0.07)	0.14 (0.03)	0.10 (0.04)	0.06 (0.004)
	$\Vert\hat{\rho}_{\kappa} - \rho_0\Vert_{L^2}/\Vert\rho_0\Vert_{L^2}$	0.32 (0.04)	0.17 (0.02)	0.14 (0.01)	0.13 (0.01)
(37)	$\Vert\hat{\rho}_{\Pi}^{(n)} - \rho_0\Vert_{L^2}/\Vert\rho_0\Vert_{L^2}$	0.47 (0.05)	0.24 (0.02)	0.14 (0.02)	0.13 (0.01)
	$\Vert\hat{\rho}_{\kappa} - \rho_0\Vert_{L^2}/\Vert\rho_0\Vert_{L^2}$	0.32 (0.03)	0.28 (0.02)	0.27 (0.006)	0.26 (0.003)

Table 4: Average relative L^2-estimation errors (and their standard deviations) over 100 repeated experiments for the posterior mean $\hat{\rho}_{\Pi}^{(n)}$ and the averaged kernel estimate $\hat{\rho}_{\kappa}$. For ρ_0 as in (36), $\Vert\rho_0\Vert_{L^2} = 9.62$; for ρ_0 as in (37), $\Vert\rho_0\Vert_{L^2} = 21.36$.

C.3 Experiments with deterministic covariates

In view of the discussion in Remark 2.5, we document the performance of our approach in an example with both random and deterministic covariates. On the spatial domain $\mathcal{W} = [-1/2, 1/2]^2$, we consider a univariate covariate random field $Z_1 = Z_{\text{rand}}$, constructed as in Section 3.1, and the deterministic covariate $Z_2(x) = Z_{\text{det}}(x) = 1/2 + x_1$ accounting for residual spatial effects in the first coordinate. On the covariate space $\mathcal{Z} = [0, 1]^2$, we take the ground truth

$$\rho_0(z_1, z_2) = \max\Big\{0, 15\ z_2\ f_{SN}(z_1, 0.8, 0.3, -5)\Big\}, \tag{38}$$

with f_{SN} the (one-dimensional) skew-normal p.d.f., cf. Figure 15, last panel.

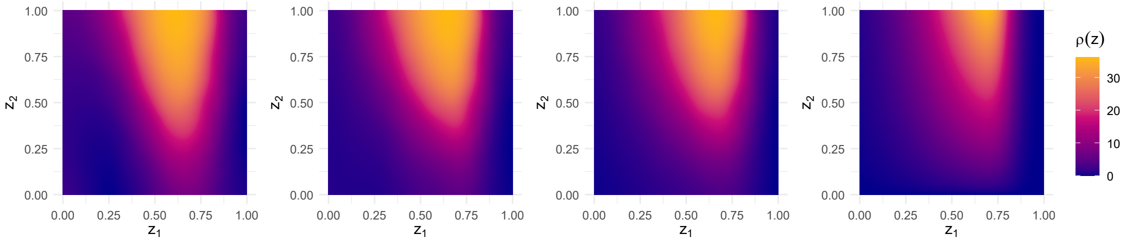

Figure 15: Left to right: Posterior means for $n = 50, 250, 1000$, and the ground truth (38).

The results are visualized in Figures 15 and 16, and summarized in Table 5. They showcase the flexibility of the proposed methods in handling both types of covariates. Particularly, the linear dependence on the first spatial coordinate is effectively detected, as shown by the projected estimates in the bottom row of Figure 16.

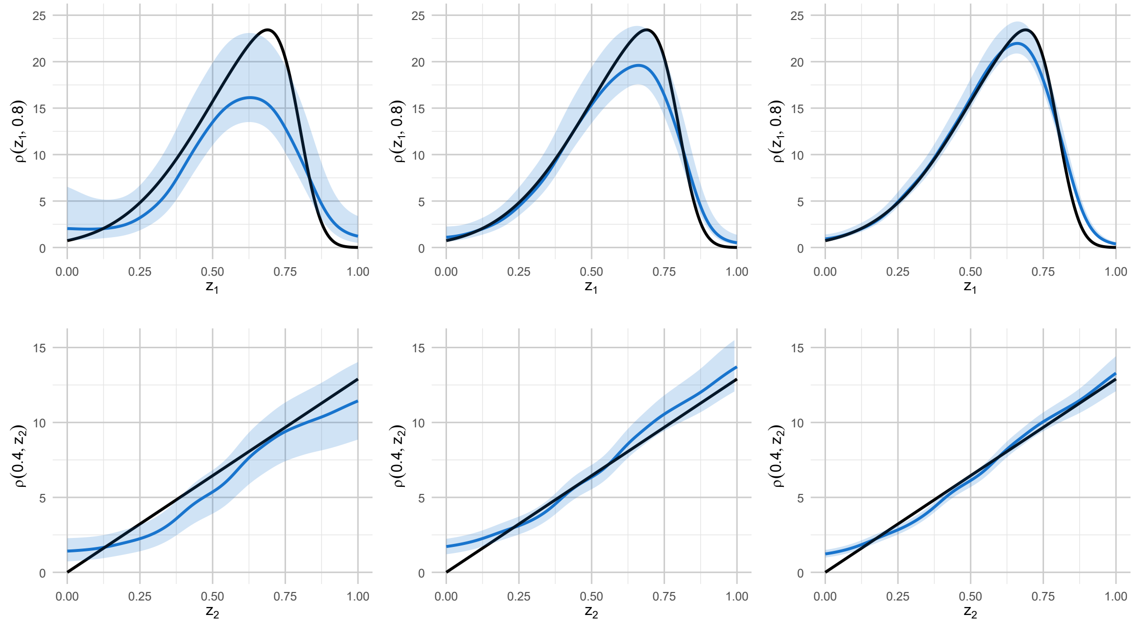

Figure 16: Top row, left to right: Projections of the posterior means (solid blue) along the subspace $z_2 = 0.8$ (i.e. $x_1 = 0.3$) and associated pointwise 95%-credible intervals (shaded blue). The solid black line represents the projection of the ground truth, $\rho_0(z_1, 0.8)$, $z_1 \in [0, 1]$, for ρ_0 as in (38). Bottom row: projections on the subspace $z_1 = 0.4$. The solid black line shows the projection $\rho_0(0.4, z_2)$, $z_2 \in [0, 1]$.

Lastly, we asses the robustness of our approach to over-parametrization by studying the effect of including an additional covariate that in reality has no effect in the true data generating mechanism. Specifically, in the experimental setup of Section 3.1, with univariate random covariate field Z_1 and ground truth (15), we fit the model

$$\lambda(x) = \rho(Z_1(x), Z_2(x)), \qquad x \in [-1/2, 1/2]^2,$$

with $Z_2(x) = 1/2 + x_1$. Figure 17 (first three panels) shows the obtained posterior means, to be compared to the 'over-parametrized' ground truth

$$\rho_0(z_1, z_2) = 5 f_{SN}(z; 0.8, 0.3, -5), \qquad z_1 \in [0, 1], \qquad z_2 = 1/2 + x_1 \in [0, 1],$$

cf. Figure 17 (last panel). The estimates capture the constant effect in the second argument (i.e., the first spatial coordinate), as can also be seen from the bottom row of Figure 18. Relative estimation errors are reported in Table 5. They are generally slightly higher than those obtained in Section 3.1, pointing to a negative impact of over-parametrization on performance.

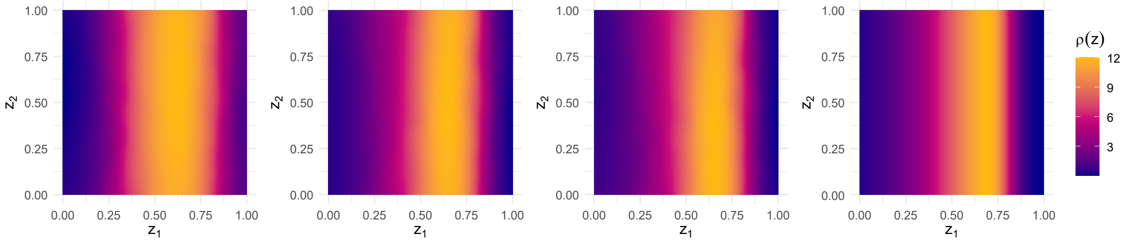

Figure 17: Left to right: Posterior means for $n = 50, 250, 1000$, and the lifted version of ground truth (15).

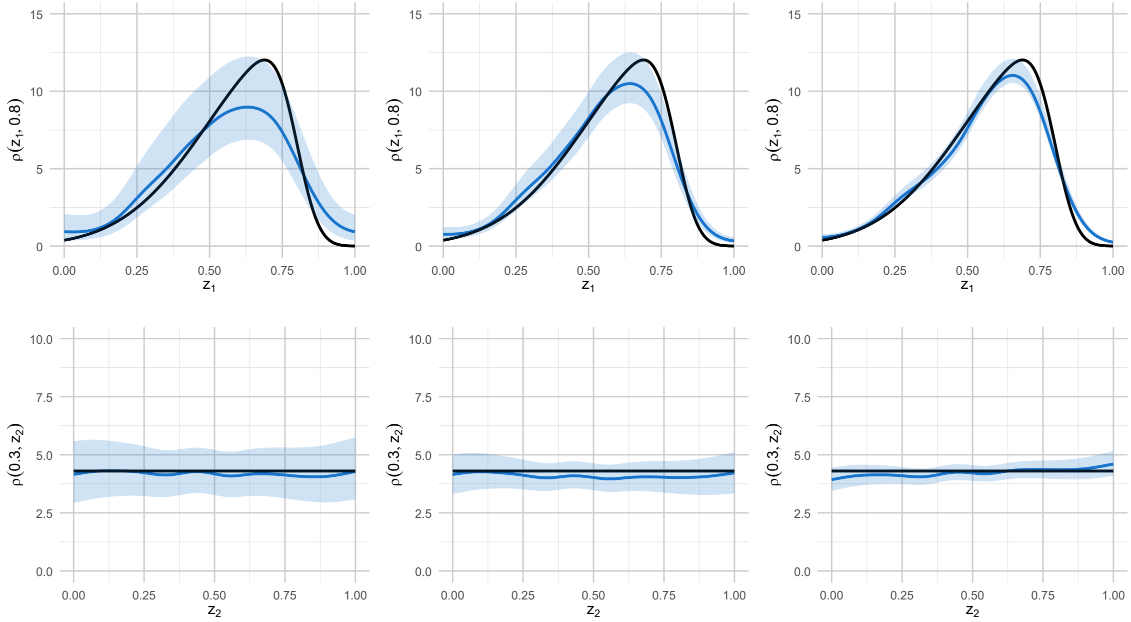

Figure 18: Top row, left to right: Projections of the posterior means (solid blue) along the subspace $z_2 = 0.8$ (i.e. $x_1 = 0.3$) and associated pointwise 95%-credible intervals (shaded blue). The solid black line represents the data generating ground truth, $\rho_0(z_1),\ z_1 \in [0, 1]$, for ρ_0 as in (15). Bottom row: projections on the subspace $z_1 = 0.3$. The solid black line shows the value $\rho_0(0.3)$.

ρ_0		$n = 10$	$n = 50$	$n = 250$	$n = 1000$
(38)	$\Vert\hat\rho_\Pi^{(n)} - \rho_0\Vert_{L^2}/\Vert\rho_0\Vert_{L^2}$	0.69 (0.03)	0.33 (0.02)	0.20 (0.02)	0.13 (0.02)
	$\Vert\hat\rho_\kappa - \rho_0\Vert_{L^2}/\Vert\rho_0\Vert_{L^2}$	0.35 (0.07)	0.29 (0.02)	0.29 (0.01)	0.28 (0.01)
(15), over-parametrized	$\Vert\hat\rho_\Pi^{(n)} - \rho_0\Vert_{L^2}/\Vert\rho_0\Vert_{L^2}$	0.62 (0.06)	0.23 (0.07)	0.14 (0.01)	0.10 (0.01)
	$\Vert\hat\rho_\kappa - \rho_0\Vert_{L^2}/\Vert\rho_0\Vert_{L^2}$	0.41 (0.07)	0.29 (0.02)	0.27 (0.01)	0.27 (0.01)

Table 5: Average relative L^2-estimation errors (and their standard deviations) over 100 repeated experiments for the posterior mean $\hat\rho_\Pi^{(n)}$ and the averaged kernel estimate $\hat\rho_\kappa$. For ρ_0 as in (38), $\Vert\rho_0\Vert_{L^2} = 7.44$.

C.4 MCMC diagnostics

Here, we document the empirical performance of the employed Metropolis-with-Gibbs MCMC algorithm in the experiments with synthetic data presented in Section 3 and above.

In the left and central panel of Figure 19, we report the trace-plots over 20000 MCMC iterations for the upper-bound ρ^* and the length-scale parameter ℓ, in the context of the one-dimensional numerical simulation study from Section 3.1. Chains in different colors refer to different experiments, each based on $n = 1000$ i.i.d. observations, and each initialized at a 'cold start' randomly drawn from the prior. The plot show consistent convergence of the chains towards equilibrium, after a burn-in period of about 5000 steps. In particular, the approximate posterior samples of ρ^* concentrate around slightly larger values than the actual maximum of the true intensity from (15) (which is equal to 12), see Fig. 2. The last panel of Figure 19 displays the trace-plots of the log-likelihood of the MCMC samples for the intensity function ρ (after the completion of each Gibbs step), seen to effectively move from the initialization point and then to stabilize around the log-likelihood of the ground truth (indicated by the dashed lines). This furnish another visualization of the convergence of the posterior distribution towards the true intensity captured by Figure 2, and also hints at the overall positive mixing behavior of the employed MCMC algorithm.

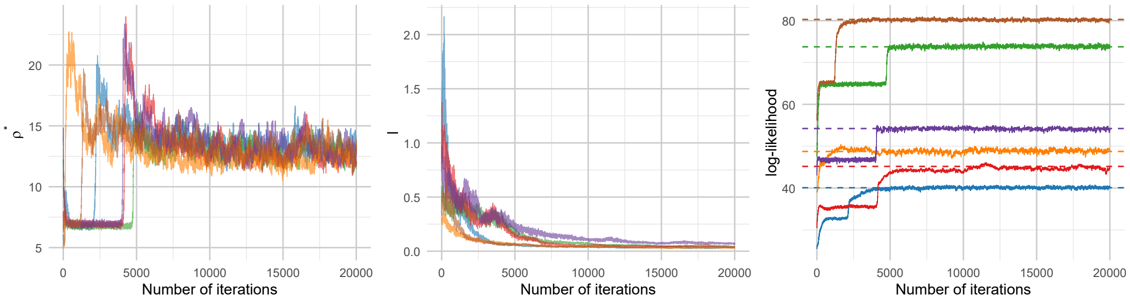

Figure 19: Left to right: Trace-plots over 20000 steps of the Metropolis-with-Gibbs MCMC algorithm for the upper bound ρ^*, the length scale parameter ℓ, and the log-likelihood of the intensity function ρ, respectively, in the one-dimensional scenario described in Section 3.1. Different colors refer to different experiments.

Figure 20 shows the trace-plots of the point-wise evaluations of the intensity function at some representative covariate levels, specifically, at the location of the maximum of the ground truth ($z = 0.65$), in the left tail ($z = 0.15$), and at the minimizer ($z = 0.95$). These are seen to stabilize around the true values $\rho_0(z)$, $z = 0.65, 0.15, 0.95$, indicated by black dashed lines.

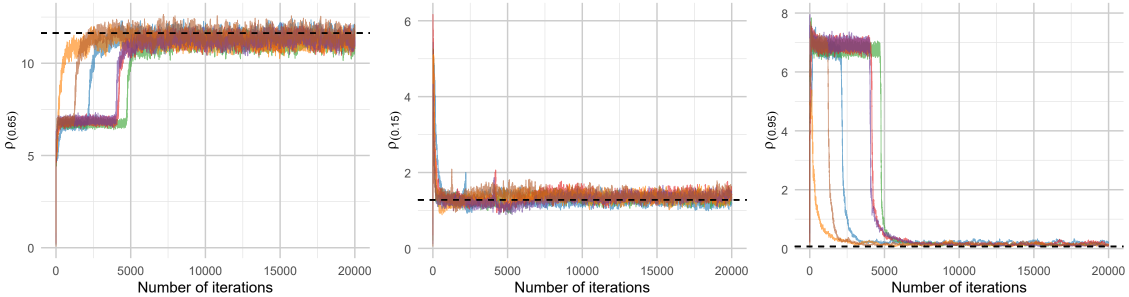

Figure 20: Left to right: Trace-plots over 20000 steps of the Metropolis-with-Gibbs MCMC algorithm for $\rho(z)$, $z = 0.65, 0.15, 0.95$, respectively, in the one-dimensional scenario described in Section 3.1. Different colors refer to different experiments.

Moving to the two-dimensional simulation study presented in Section 3.2, recall the anisotropic ground truth from (16), whose characteristic length-scale in the first argument is around one order of magnitude smaller than in the second. Figure 21 displays the trace-plots for the upper bound parameter ρ^*, the two length-scales ℓ_1, ℓ_2, their exponents θ_1,θ_2, as well as for the log-likelihood after each complete Gibbs step. In our nonparametric Bayesian procedure, the length scales relative to distinct directions are allowed to vary independently, and we observe that the corresponding chains stabilize (despite some variability across the experiments) around values that differ by a factor close to 10, reflecting the anisotropy of the true intensity function.

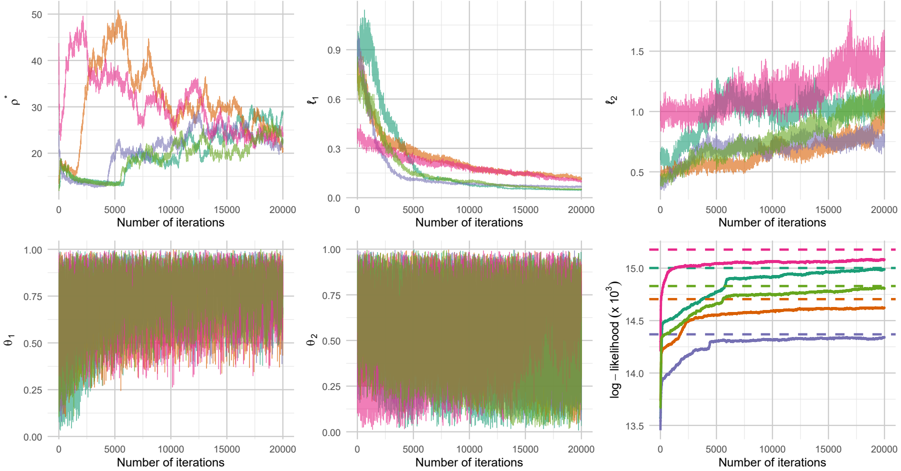

Figure 21: Left to right, top to bottom: Trace-plots over 20000 steps of the Metropolis-with-Gibbs MCMC algorithm for various parameters and for the log-likelihood (last panel; dashed lines indicate the log-likelihood of the ground truth), in the two-dimensional scenario described in Section 3.2. Different colors refer to different experiments. The sample size is $n = 1000$ across all experiments.

We conclude with a brief comparison of the last set of runs to those relative to the bi-variate numerical simulation studies with isotropic ground truth ρ_0 from (36); see Section C.2. In this case, the posterior distributions of the length-scale parameters ℓ_1, ℓ_2 appear to concentrate over the same region, as shown by the trace-plots reported in Figure 22. In line with the theoretical findings from Section 2.2, which provide optimal posterior contraction rates also in the case of isotropic true intensities, this illustrates the ability of the proposed methods to flexibly adapt to the the intrinsic structural features of the ground truth.

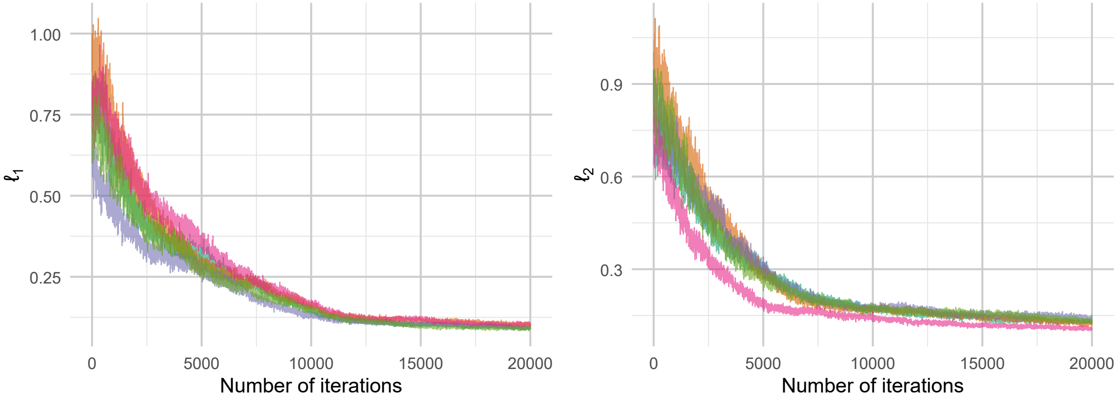

Figure 22: Left to right, top to bottom: Trace-plots over 20000 steps of the Metropolis-with-Gibbs MCMC algorithm for the length-scale parameters ℓ_1, ℓ_2, in the two-dimensional scenario with ground truth ρ_0 from (36) described in Section 3.2. Different colors refer to different experiments. The sample size is $n = 1000$ across all experiments.

D Expanded applications to the Canadian wildfire dataset

In this appendix, we expand the application to the Canadian wildfire dataset developed in Section 4. We present additional analyses for the province of Ontario, cf. Sections 4.1 and 4.2, and report the obtained plug-in posterior means of the yearly spatial intensity for a broader selection of years. Moreover, we repeat the workflow for the provinces of Saskatchewan, in the central region of Canada, and British Columbia, on the Western coast.

D.1 Further results for the Ontario dataset

In addition to the exploratory univariate analysis from Section 4.1 and the full one from Section 4.2, we also fit a model jointly based on the temperature and the precipitation level, which our investigations, in accordance with the literature, e.g. Borrajo et al. (2020), indicate as the two meteorological factors with the greatest influence on the risk of wildfires. In Figure 23, we plot the obtained posterior mean (in the central panel) and averaged kernel estimate (on the right). These broadly agree in shape and magnitude, placing greater intensities in correspondence of higher temperatures and drier conditions. These findings are similar to the ones from the full analysis from Section 4.2, cf. Figure 7, where the inclusion of the average wind speed as an additional covariate was observed to impact the overall intensity level, but to generally preserve the distribution of the risk across the covariate space.

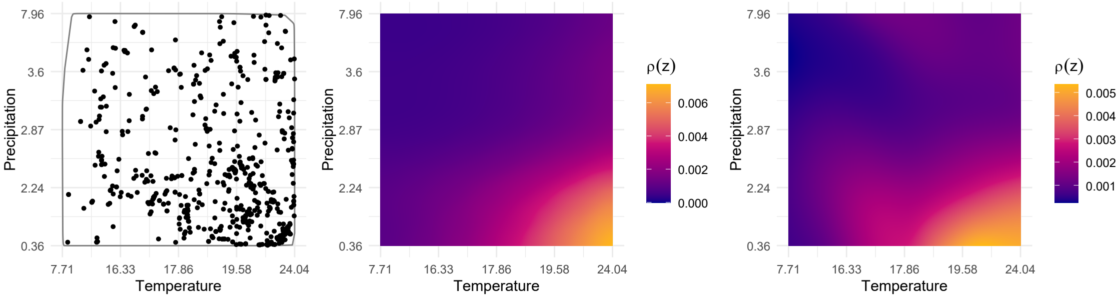

Figure 23: Left panel: Average temperatures and precipitation levels at each location in Ontario where a wildfire has been detected in the considered time period. Central panel: Posterior mean of the wildfire intensity as a function of the two covariates. Right panel: Averaged kernel estimate.

Returning to the full analysis based on temperature, precipitation level and wind speed, cf. Section 4.2, in Figure 24 we display six additional plug-in posterior means of the yearly spatial intensity for a broader selection of years across the time period, specifically for 2006, 2008, 2010, 2016, 2018, 2022. Note that, for visual clarity of the individual plots, the color scales differ across the panels. Years with a small number of wildfires, like 2008 and 2010 (second and third panel, respectively), are generally assigned low intensities, with local peaks possibly associated with events.

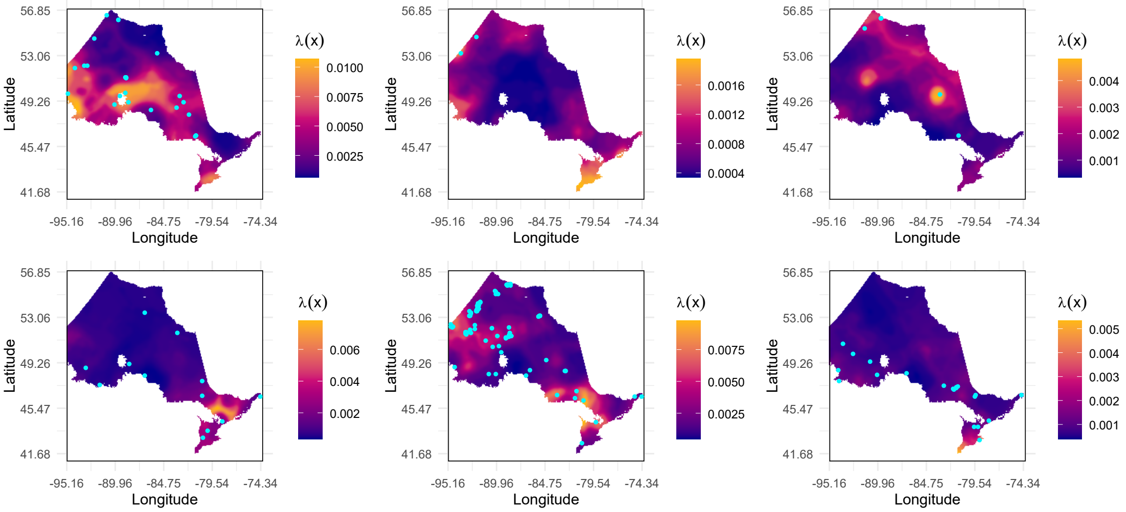

Figure 24: Left to right, top to bottom: Plug-in posterior means of the spatial intensity as a function of the location-specific average temperature, precipitation level and wind speed in Ontario, for the years 2006, 2008, 2010, 2016, 2018, 2022.

D.2 Results for the Saskatchewan datasets

The dataset for the provinces of Saskatchewan and British Columbia are structured similarly to the one for Ontario described in Section 4, each comprising $n = 19$ spatial point patterns with the aggregate locations of wildfires detected in June over the time period from 2004 to 2022, and as many tri-dimensional spatial covariate fields with the coordinate-specific average temperatures, precipitation levels and wind speeds.

An illustration of the data for Saskatchewan is presented in Figure 25. Similar to Section 4, we observe some strong variability in the yearly number of events, as well as in the range and fluctuations of the covariates.

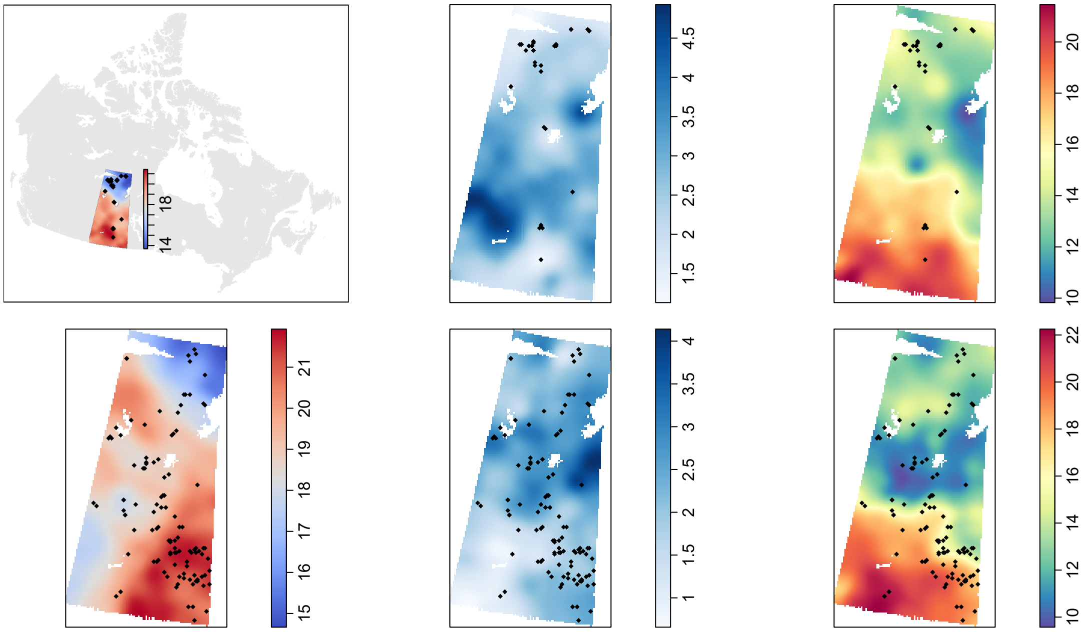

Figure 25: Top row, left to right: Average temperatures (in Celsius), precipitations (in mm/m^2) and wind speeds (in km/h) in Saskatchewan during June 2013. Bottom row: Observations for 2021. The wildfires are represented by black dots (respectively, 40, and 114 in total).

We again first perform a preliminary analysis, separately studying the influence of each individual covariate on the wildfire intensity. The results are shown in Figure 26. Consistently with the behavior observed in Section 4, the temperature-based posterior mean displays a strong positive association, with a sharp raise between 16°C and 25°C. Also, a heavy negative impact of rains, particularly above 1 mm/m^2, is again captured. Minor differences emerge for the wind speeds, where a peak is located around 13 km/h, similarly to Figure 5 (right panel), but overall higher intensities are detected in the left tail than in the right one. This suggests the presence of some potential heterogeneity in the way in which wind speeds effect the risk of wildfires across different regions in Canada. The results for the full analysis, based on the joint information on all three covariates, are also in line with those presented in Section 4.2. For brevity, we only display the obtained spatial plug-in posterior means, for the same selection of years 2006, 2008, 2010, 2013, 2015, 2016, 2018, 2021 and 2022. See Figure 27.

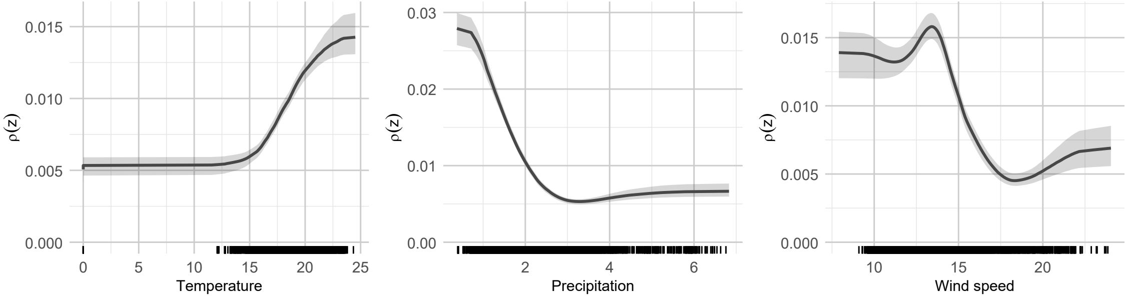

Figure 26: Left to right: Posterior means (solid black) of the wildfire intensity as a function of the average temperature, precipitation level and wind speed, respectively, in Saskatchewan. The shaded regions indicate point-wise 95%-credible intervals.

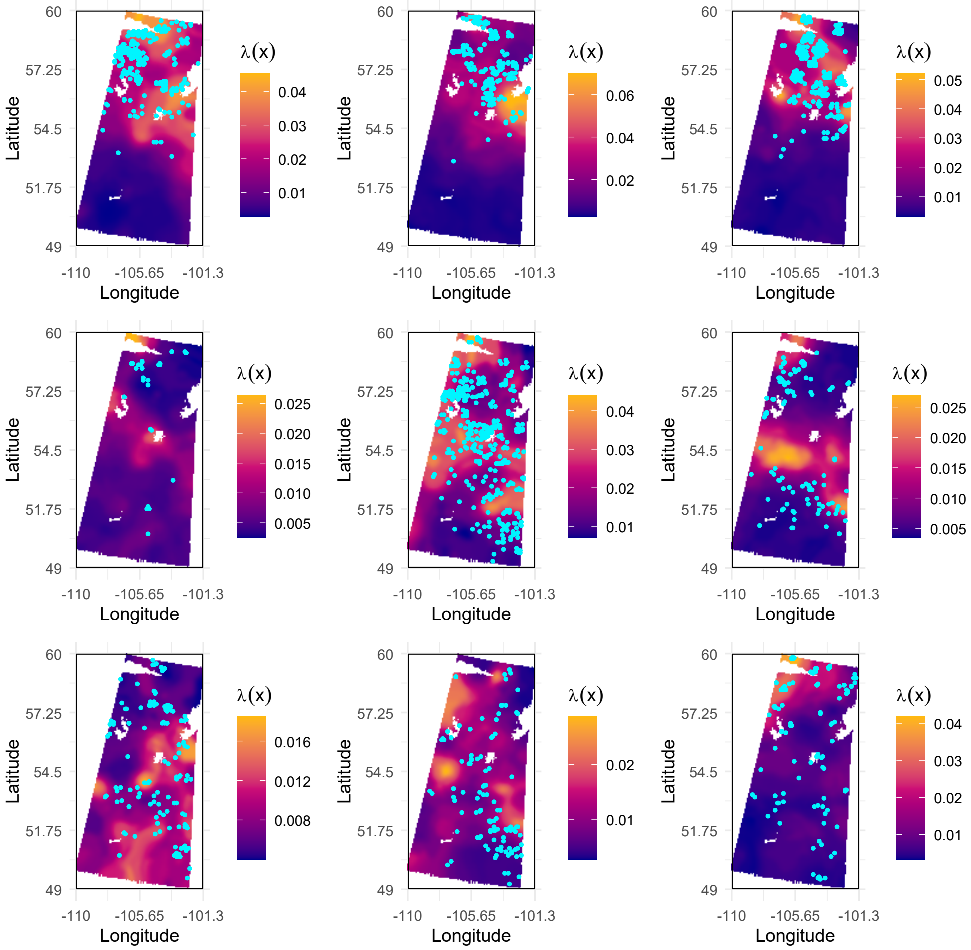

Figure 27: Left to right: Plug-in posterior means of the spatial intensity in Saskatchewan based on average temperature, precipitation level and wind speed, for the years 2006, 2008, 2010, 2013, 2015, 2016, 2018, 2021 and 2022.

D.3 Results for the British Columbia dataset

We conclude with a summary of the obtained results for the British Columbia dataset. Figure 28 showcases two individual observations of the events and covariates. The exploratory posterior means individually based on each covariate are displayed in Figure 29, closely aligned to ones relative to the other two provinces, cf. Figures 5 and 26. The plug-in posterior means for the yearly spatial intensity are shown in Figure 30, resulting from the full analysis based on the joint meteorological information.

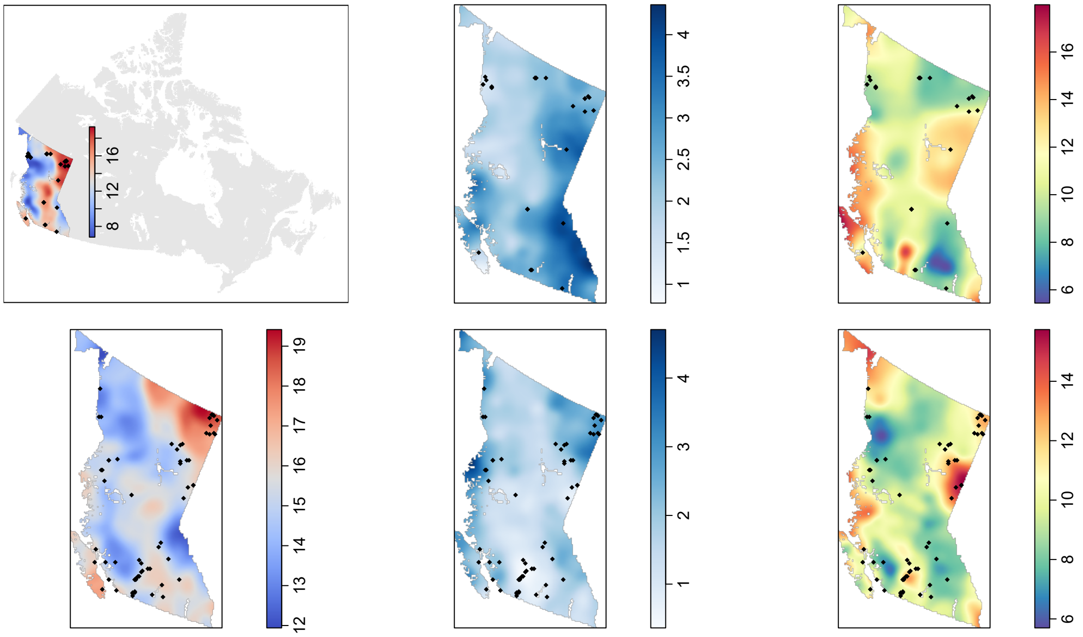

Figure 28: Top row, left to right: Average temperatures (in Celsius), precipitations (in mm/m^2) and wind speeds (in km/h) in British Columbia during June 2013. Bottom row: Observations for 2021. The wildfires are represented by black dots (respectively, 28, and 64 in total).

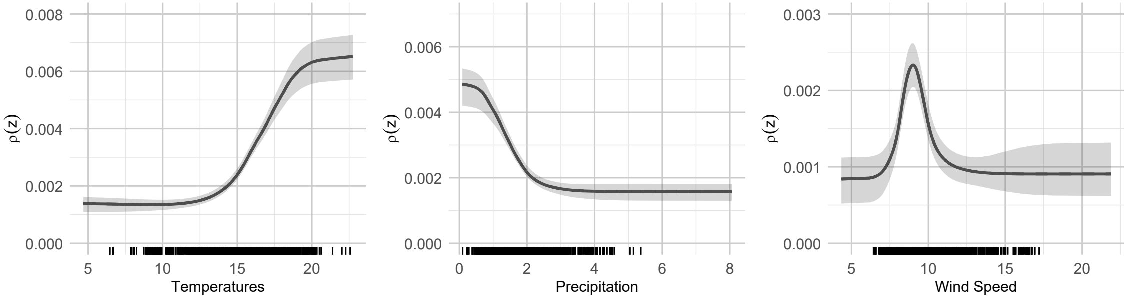

Figure 29: Left to right: Posterior means (solid black) of the wildfire intensity as a function of the average temperature, precipitation level and wind speed, respectively, in British Columbia. The shaded regions indicate point-wise 95%-credible intervals.

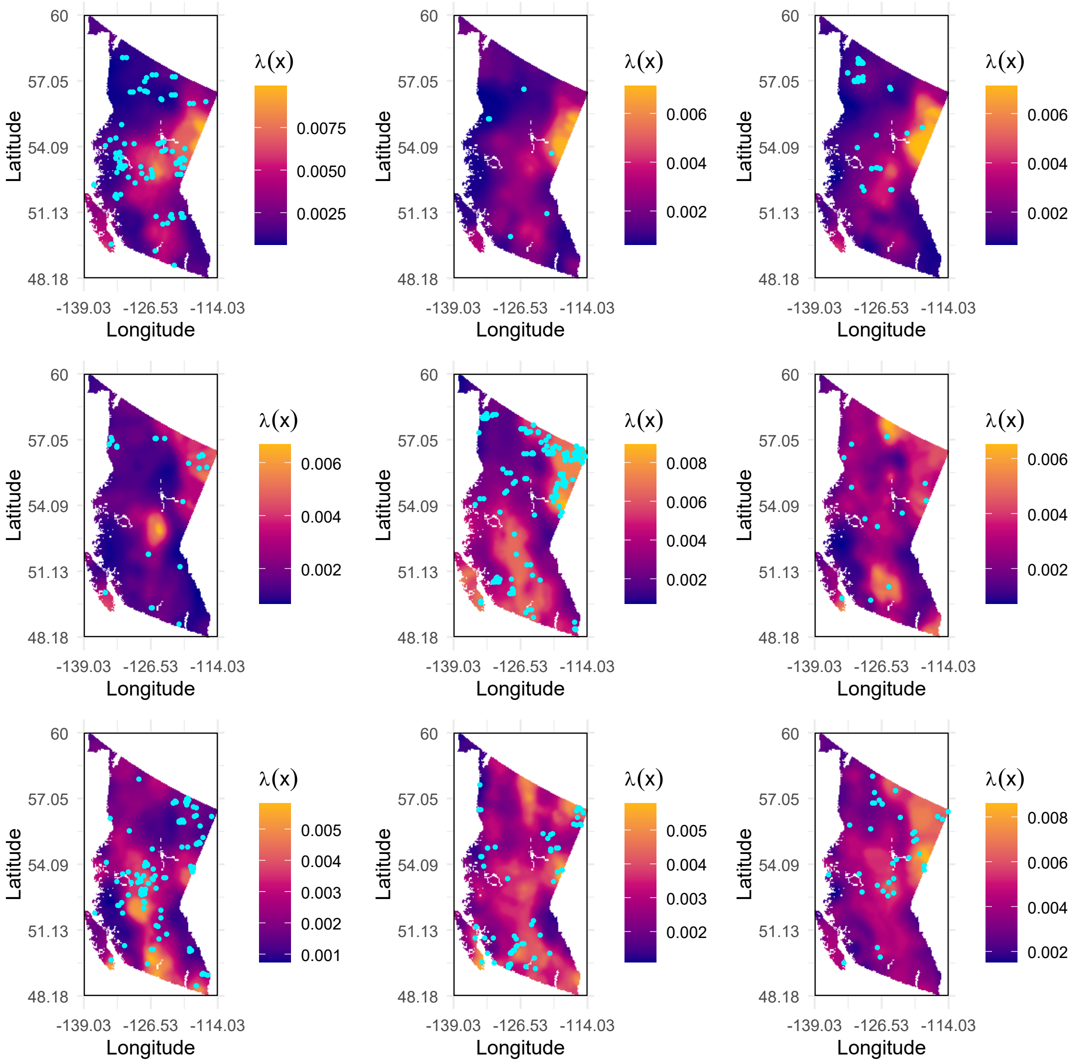

Figure 30: Left to right: Plug-in posterior means of the spatial intensity in British Columbia as a function of the location-specific average temperature, precipitation level and wind speed, for the years 2006, 2008, 2010, 2013, 2015, 2016, 2018, 2021 and 2022.